

INFORMATION TO USERS

This manuscript has been reproduced from the microfilm master. UMI films the text directly from the original or copy submitted. Thus, some thesis and dissertation copies are in typewriter face, while others may be from any type of computer printer.

The quality of this reproduction is dependent upon the quality of the copy submitted. Broken or indistinct print, colored or poor quality illustrations and photographs, print bleedthrough, substandard margins, and improper alignment can adversely affect reproduction.

In the unlikely event that the author did not send UMI a complete manuscript and there are missing pages, these will be noted. Also, if unauthorized copyright material had to be removed, a note will indicate the deletion.

Oversize materials (e.g., maps, drawings, charts) are reproduced by sectioning the original, beginning at the upper left-hand corner and continuing from left to right in equal sections with small overlaps. Each original is also photographed in one exposure and is included in reduced form at the back of the book.

Photographs included in the original manuscript have been reproduced xerographically in this copy. Higher quality 6" x 9" black and white photographic prints are available for any photographs or illustrations appearing in this copy for an additional charge. Contact UMI directly to order.

UMI

A Bell & Howell Information Company
300 North Zeeb Road, Ann Arbor MI 48106-1346 USA
313/761-4700 800/521-0600

**MERGING REMOTELY SENSED DATA WITH GEOPHYSICAL
MODELS**

A

THESIS

Presented to the Faculty
of the University of Alaska Fairbanks
in Partial Fulfillment of the Requirements
for the Degree of

DOCTOR OF PHILOSOPHY

By

Stanley Craig Searcy, B.S., M.S.

Fairbanks, Alaska

August 1996

UMI Number: 9632228

UMI Microform 9632228
Copyright 1996, by UMI Company. All rights reserved.

**This microform edition is protected against unauthorized
copying under Title 17, United States Code.**

UMI
300 North Zeeb Road
Ann Arbor, MI 48103

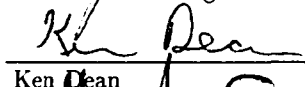
MERGING REMOTELY SENSED DATA WITH GEOPHYSICAL
MODELS

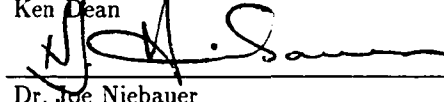
by

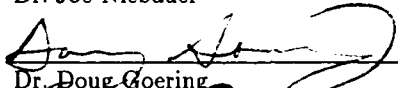
Stanley Craig Searcy

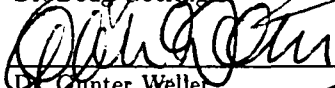
RECOMMENDED:

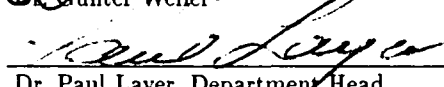

Dr. William Stringer


Ken Dean


Dr. Joe Niebauer

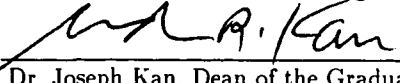

Dr. Doug Goering


Dr. Gunter Weller


Dr. Paul Layer, Department Head
Dept. of Geology and Geophysics

APPROVED:


Dr. Paul Reichardt, Dean, College of Natural Sciences


Dr. Joseph Kan, Dean of the Graduate School

6/21/96
Date

Abstract

Geophysical models are usually derived from the idealistic viewpoint that all required external parameters are, in principle, measurable. The models are then driven with the best available data for those parameters. In some cases, there are few measurements available, because of factors such as the location of the phenomena modeled. Satellite imagery provides a synoptic overview of a particular environment, supplying spatial and temporal variability as well as spectral data, making this an ideal source of data for some models. In other cases, although frequent satellite image observations are available, they are of little use to the modeler, because they do not provide values for the parameters demanded by the model. This thesis contains two examples of geophysical models that were derived expressly to utilize measurements and qualitative observations taken from satellite images as the major driving elements of the model. The methodology consists of designing a model such that it can be 'run' by numerical data extracted from image data sets, and using the image data for verification of the model or adjustment of parameters. The first example is a thermodynamic model of springtime removal of nearshore ice from an Arctic river delta area, using the Mackenzie River as a study site. In this example, a multi-date sequence of AVHRR images is used to provide the spatial and temporal patterns of melt, allowing the required physical observations in the model to be parameterized and tested. The second example is a dynamic model simulating the evolution of a volcanic ash cloud under the influence of atmospheric winds. In this case, AVHRR images are used to determine the position and size of the ash cloud as a function of time, allowing tuning of parameters and verification of the model.

Contents

Abstract	iii
List of Figures	viii
Preface	x
1 Introduction	1
References	3
2 Merging remotely sensed data with geophysical models	4
2.1 Introduction	4
2.2 Methodology	5
2.3 Case Studies	7

3 A river-coastal sea ice interaction model: Mackenzie River Delta¹	9
Abstract	9
3.1 Introduction	10
3.2 Background	11
3.2.1 The Breakup Dynamics	11
3.2.2 Satellite Imagery	13
3.3 Analysis	14
3.3.1 Sensible Heat	15
3.3.2 Radiative Transfer	16
3.4 The River-Ice Interaction Model	17
3.4.1 The Upper Surface Heat Balance	17
3.4.2 The Riverine Heat Flux	19
3.4.3 Discussion of the River Parameters	20
3.5 Results and Conclusions	23
Appendix	26
Acknowledgments	27

¹published as: Searcy, C., K. Dean, and W. Stringer (1996). A river-coastal sea ice interaction model: Mackenzie River Delta, *J. Geophys. Res.* 101 (C4), 8885-8894

References	27
Figures	30
4 PUFF: A high resolution volcanic ash tracking model²	42
Abstract	42
4.1 Introduction	43
4.2 Model Background	45
4.2.1 Wind Data and Transport	47
4.2.2 Turbulent Dispersion	48
4.2.3 Fallout	50
4.3 Model Description	50
4.3.1 Ash Particle Initialization	52
4.4 Case Studies	54
4.4.1 1992 Mount Spurr/Crater Peak Eruptions	54
4.4.2 Klyuchevskoy Volcano, October 1994	58
4.4.3 Rabaul Caldera, September 1994	60
4.5 Conclusions	62

²submitted as: Searcy, C., K. Dean, and W. Stringer, *Journal of Volcanology and Geothermal Research*, May 1996

	vii
Acknowledgments	62
References	63
Figures	66
5 Discussion	80
5.1 Nearshore Ice Removal, Mackenzie River Delta	80
5.1.1 Satellite Observations and Model Development	81
5.1.2 Satellite Observations and Model Parameters	82
5.2 A Dynamic Model of Volcanic Ash Dispersion	84
5.2.1 Satellite Observations and Diffusivity	84
5.2.2 Satellite Observations and Plume Heights	86
6 Summary	91
A The PUFF System Manual	93
THE PUFF SYSTEM	96
THE PUFF MAN PAGES	99

List of Figures

3.1	Map of the study region	31
3.2	Schematic diagram of the 1986 visible band AVHRR images	32
3.3	Comparison of the river discharge to areal measurements	33
3.4	Average albedo measurements	34
3.5	Schematic diagram of the idealized model region	35
3.6	Atmospheric heat fluxes	36
3.7	Ice decay curves	37
3.8	A comparison of the net heat flux	38
3.9	The fraction of the total energy supplied by the river	39
3.10	The influence of river melting start date on the ice decay	40
3.11	The fraction of the total energy supplied by the river by start date	41

4.1	North Pacific area map	67
4.2	Three possible vertical plume distributions	68
4.3	Two ash size distributions	69
4.4	Mount Spurr AVHRR thermal infrared images	70
4.5	Mount Spurr temperature profile	71
4.6	Mount Spurr wind vectors	72
4.7	Mount Spurr ash trajectories	73
4.8	Mount Spurr PUFF simulation	74
4.9	Mount Spurr PUFF simulation mosaic	75
4.10	Klyuchevskoy Volcano AVHRR thermal infrared image and PUFF simulation	76
4.11	Klyuchevskoy Volcano wind vectors	77
4.12	Rabaul Caldera AVHRR thermal infrared image and PUFF simulation . .	78
4.13	Rabaul Caldera wind vectors	79
5.1	AVHRR images of the Mackenzie River delta, April/May 1986	87
5.2	AVHRR images of the Mackenzie River delta, June 1986	88
5.3	AVHRR images of the Mackenzie River delta, July/August 1986	89
5.4	AVHRR imagery of the August 1992 Mount Spurr eruption and simulations	90

Preface

This thesis consists of a body of work which I have produced while in the doctoral program at the Geophysical Institute, University of Alaska Fairbanks. The content of the thesis includes two manuscripts in their original form and a technical manual as an appendix. Of the two manuscripts, one is published while the other has been submitted for publication and is in the review process as of this writing.

Each chapter containing a published or submitted manuscript appears in its entirety including abstract, list of figures, and references. Figures for each are included at the end of the chapter as they were in originally submitting the documents. The list of figures at the beginning of the thesis includes all figures, while each chapter contains a separate list. References are found at the end of the chapter text and include only those cited in the document. The section, figure and equation numbers are preceded by the chapter number as in figure 2.1 for figure 1, chapter 2.

Chapter 1

Introduction

The thesis subject matter, *Merging remotely sensed data with geophysical models*, came about from combining two projects that I have worked on into a single coherent thesis. The first project investigated and modeled the contribution of a major arctic river to the early melting of coastal sea ice in its vicinity. The second project developed a model for the simulation and tracking of volcanic ash clouds and resulted in operational software used at the Geophysical Institute and the National Weather Service in Anchorage, AK. While these two projects vary in subject matter, the detail and content were similar. Both projects resulted in a numerical model of a specific geophysical process and both relied on the use of satellite imagery either in the initial development of the model or for validation and verification of model results.

When the topic of merging remotely sensed data with numerical models was proposed as the subject matter for this thesis, I began to develop an approach and methodology that I used in the two projects. This became the basis for a talk I presented at *Third Circumpolar Symposium on Remote Sensing of Arctic Environments*, Fairbanks, Alaska, May 1994. Later, the presentation was formally written and published as *Merging remotely*

sensed data with geophysical models [Searcy et al., 1995]. That manuscript now stands as the subject matter for this thesis. Chapter 2 repeats the introductory material from that manuscript. Chapters 3 and 4 present the two case studies discussed in that manuscript in their complete, 'stand-alone' published or submitted form. Chapter 5 continues the discussion of the two case studies within the context of merging remotely sensed data with geophysical models.

Chapter 3, *A river-coastal sea ice interaction model: Mackenzie River Delta*, presents the first of the two case studies in its published form [Searcy et al., 1996b]. The secondary authors, Ken Dean and William Stringer, contributed to the paper in the form of guidance, consultation and funding by authoring the initial grant proposal. The model described is original work of my own. The project investigated the influence of a major arctic river to the early removal of coastal sea ice observed in its vicinity. The influence of discharge was quantified using a theoretical development and satellite imagery as a data base. The model also allowed for predicting possible influences due to the removal of the ice resulting from alterations in river discharge patterns. An additional manuscript, not included here since I had only a minor contribution to the manuscript, was also published as part of this project [Dean et al., 1994].

Chapter 4, *PUFF: A high resolution volcanic ash tracking model*, presents the second project in its submitted form [Searcy et al., 1996a]. As in the first case, the secondary authors, Ken Dean and William Stringer, contributed in the form of guidance, consultation and funding and the model described is original work of my own. This project developed a model for the simulation and tracking of volcanic ash clouds. Satellite imagery was used to verify and validate the model's accuracy and 'fine-tune' model parameters. Additionally, the project developed software tools sufficient for use in an operational environment, requiring a significant effort beyond the scope of the model itself. This effort is represented by the inclusion of the technical manual as an appendix.

References

- Dean, K., W. Stringer, K. Ahlnaes, S. Searcy, and T. Weingartner (1994). The influence of river discharge on the thawing of sea ice: Mackenzie River Delta: albedo and temperature analysis. *Polar Res.* 13, 83–94.
- Searcy, C., K. Dean, and W. Stringer (1995). Merging remotely sensed data with geophysical models. *Polar Record* 31(178), 297–304.
- Searcy, C., K. Dean, and W. Stringer (1996a). Puff: A high resolution volcanic ash tracking model. submitted to *Journal of Volcanology and Geothermal Research*, May 1996.
- Searcy, C., K. Dean, and W. Stringer (1996b). A river-coastal sea ice interaction model: Mackenzie River Delta. *J. Geophys. Res.* 101(C4), 8885–8894.

Chapter 2

Merging remotely sensed data with geophysical models

2.1 Introduction

The modeling of geophysical phenomena requires either a direct knowledge or estimation of specific physical parameters. In the absence of any collected data, these parameters may have only a theoretical basis for their values. Satellite imagery provides a synoptic, quantitative and qualitative data set which can set certain model parameters, aid in the initial development of models and validate model results. This paper discusses some of the methodology used when incorporating imagery into model parameters. Two examples are presented. The main contribution of satellite imagery to modeling is the spatial variability, temporal variability and spectral composition of the data set. The spatial and temporal components provide qualitative as well as quantitative data which can be exploited in the design of the model. This leads to a model that is well grounded in observable and measurable quantities and relies less on theoretical assumptions. Satellites record data

over a variety of wavelength bands, each of which provides specific information. Spectral data can be used to set numerical parameters in the model or as an objective verification of model predictions by a direct numerical comparison. This of course assumes that the images have been calibrated on some absolute scale for the extraction of raw numerical data. In other cases, due to measurement errors or assumptions, the data may only impose limits on the parameters. Model 'tuning' may be required by varying parameter values over successive runs until model results agree reasonably well with observations.

Some limitations exist, however, with the use of imagery in numerical models. Most imagery is dependent on weather and environment and may not be useful in a particular situation. Extracting numerical data from images usually requires calibration. This can be either absolute or relative depending on the needs of the model. There may be additional assumptions or models required for interpreting the data, for example, atmospheric corrections. Field measurements or observations may also be necessary for confidence in image interpretation.

2.2 Methodology

Imaging satellite sensors record data that have spatial, temporal and spectral components. The spatial information indicates the position and shape of surface features that can be measured precisely. The temporal information indicates surface conditions at specific times. The spectral information provides quantitative values such as temperature or albedo if the data are calibrated. All this information is available back to the early 1970's or in some cases earlier. However, some of the older digital data have been lost and it may be difficult to calibrate spectral values in what remains. There can also be problems in cross-platform data calibration.

Satellite data recorded by the NOAA Advanced Very High Resolution Radiometer

(AVHRR) sensor are used in the examples described in this paper. Images from the AVHRR sensor aboard polar orbiting satellites have a spatial resolution of 1 km and a swath width greater than 2000 km. There are at least two NOAA satellites in opposing orbits recording imagery at the equator every six hours. At high latitudes data are recorded almost once per hour, although the observing times are not linearly distributed over 24 hours. Spectrally, these data are recorded in five wavelengths: visible band 1 (0.58 - 0.68 μm), near-infrared band 2 (0.72 - 1.1 μm), thermal infrared band 3 (3.55 - 3.93 μm) thermal infrared band 4 (10.3 - 11.3 μm) and thermal infrared band 5 (11.5 - 12.5 μm). Albedo values are derived from visible and near-infrared bands and temperature values are given by the thermal bands.

Models begin with a design phase in which the developer attempts to describe the important physical processes in the system being modeled. Some physical models can be designed using theoretical principles alone and empirical models require only statistical data. In most cases however, only certain physical laws (such as conservation of energy or momentum) determine if the model behaves properly. Model complexity can range from a simple predictive analytical equation to a highly sophisticated numerical integration technique. A sophisticated and complex numerical model may not actually provide any more information than a simpler one. It could also be much more difficult to directly verify a model if there is no relevant output to compare with observations. The developer should consider the data set and emphasize specific properties in the model, without ignoring other, less-known variables that are important to the process. This can be accomplished by paying particular attention to such things as spatial patterns, timing constraints and quantitative information acquired from imagery. By incorporating a reference data set in the initial design of the model, the developer will then be better able to validate the simulation with observations. Satellite imagery provides an excellent reference data set for some types of models.

The ideal model would have specific observable information available for every input

parameter. In reality, many parameters are ill-defined and require several assumptions about their physical state. In the best case, satellite imagery can provide raw numerical data for some parameters. Another use of imagery is to allow a subjective analysis, leading to better estimations of less-known parameters. Once a model is designed and implemented with all inputs specified, it remains to be tested for valid results. Satellite imagery provides another data set for validating model predictions. Again, in the ideal case, this would be a numerical comparison of predictable quantities to measured data. Imagery may, however, only impose limits on the observables, such as the timing of certain events or a specific range of values. A subjective verification may be all that is available to validate a model in the absence of better or more data. Subjective verification is meant in this context as a visual check of the model results to see if it 'looks about right', that is, if spatial or textural patterns appear to fit observations.

The final aspect of merging satellite data with models is 'model tuning'. This is related to the subject of validation in that this process requires a comparison of model results with the data set. 'Tuning' allows the estimation of the less well-known parameters. By varying certain parameter values over successive runs through a 'feed-back' procedure, their value can be estimated using the best agreement with observations. This assumes other variables required by the model are well-defined, otherwise competing effects of the parameters could confuse the interpretation.

2.3 Case Studies

Two case studies are presented here as an illustration of these ideas. Each is a separate study and is reproduced in chapters 3 and 4 in their original form. Chapter 3 represents a thermodynamic model of the interaction between river discharge and nearshore ice. Chapter 4 is a dynamic model of the atmospheric dispersion of a volcanic ash cloud.

While the subjects vary considerably, each represents a case where certain data acquired from satellite imagery are required by the model. The imagery provides the data for input as well as for validation of the models. The presentation of the models in each chapter does not explicitly discuss these concepts, since each is written to focus on the model itself. Following the presentation of the two models, chapter 5 includes a discussion of the models in the context of the thesis topic.

Chapter 3

A river-coastal sea ice interaction model: Mackenzie River Delta¹

Abstract

It has been observed that arctic coastal regions which receive river discharge show significant ice regression in advance of other coastal areas without this source of sensible heat. This phenomena has been particularly apparent on satellite imagery. The work reported here 1) attempts to quantify and assess the influence of spring-time river discharge on the removal of nearshore ice, and 2) demonstrate the utility of satellite imagery as a source of data to 'drive' a model assessing the influence of spring-time river discharge on the removal of nearshore ice. Central to this work is a sequence of AVHRR images of the Mackenzie Delta region, North West Territories, Canada. These images constitute a data base establishing the temporal sequence of observable breakup events from which a thermodynamic model for the ice decay can be parameterized. The emphases of this model is the influence of the riverine sensible heat on the melting of sea ice, and the ability of satellite imagery to monitor this process. For simplicity, climatological values rather than meteorological values for atmospheric and solar influences have been used. The results suggest that the river discharge supplies a significant amount of sensible heat to the base of the nearshore ice, accounting for nearly half of the energy required to melt the ice cover. As a result, the coastal ice is removed 7-14 days in advance of areas without significant river discharge.

¹published as: Searcy, C., K. Dean, and W. Stringer (1996). A river-coastal sea ice interaction model: Mackenzie River Delta, *J. Geophys. Res.* 101 (C4), 8885-8894

3.1 Introduction

Sea ice is an important component in arctic climate research since it acts as an insulating barrier between the ocean and atmosphere by limiting the transfer of heat, moisture, and momentum. Freshwater input to the Arctic Basin indirectly interacts with the perennial pack ice cover through the upper layer temperature and salinity structure. Several authors have studied the impact of altering the Arctic Ocean freshwater budget in response to earlier proposed Soviet river diversions [Aagard and Coachman, 1975; Semtner Jr., 1984; Micklin, 1981]. These studies focused on the stability of the upper water column in the Arctic Basin and whether it is maintained by the freshwater budget. The stable stratification effectively prevents a source of heat contained in deeper 'Atlantic layer' from interacting with the ice cover. Aagard and Coachman [1975] argued that reducing the amount of freshwater influx would eventually erode the stable layer allowing deep oceanic convection to sustain large fluxes of heat to the surface and thus prolong ice-free conditions. However, the numerical model of Semtner Jr. [1984] showed no deep convection occurring as a result of altering the freshwater input and hence no significant change to the state of the sea ice.

While the entire Arctic Basin may or may not be particularly sensitive to the overall freshwater budget, arctic rivers and streams interact directly with the nearshore ice cover, supplying a significant source of sensible heat to this region. Coastal regions receiving river discharge show significant ice regression in advance of other areas along the coast, presumably as a result of this introduced heat. As long as it is in place, the nearshore ice cover acts as an insulating barrier between the marine environment and the atmosphere and hence influences local climate. Alterations to the volume or timing of river discharge due to possible climatic warming could have a pronounced effect on the timing and areal extent of the degradation of the ice cover. As the process of ice removal occurs very near the summer solstice when short-wave input is at a maximum, extending the amount of

open water prior to this time could lead to further climatic change through a positive albedo-temperature feedback mechanism.

For this study, a temporal sequence of Advanced Very High Resolution Radiometer, (AVHRR) imagery was acquired for the 1986 spring breakup season in the Mackenzie River delta, NWT, Canada. These images establish the areal extent of the ice cover and the timing of certain breakup events. This data set becomes the basis for a thermodynamic ice model attempting to parameterize the convective heat transfer from the river discharge to the base of the ice cover. The model also includes a surface heat balance with short and longwave radiation as well as sensible and latent heats. Such a model predicts the removal of the ice cover as a result of thermal forcing on its two horizontal surfaces.

The chief objective of this study is to make a first order determination of the influence of the river discharge on ice removal. For the purpose of this 'sensitivity test', we chose to simplify the model by using climatological values for atmospheric and solar influences rather than actual meteorological values. Clearly, the next step in this development would be achieved by extending the model to be driven by actual meteorological values.

3.2 Background

3.2.1 The Breakup Dynamics

The thawing of rivers in the western Arctic occurs in late spring when sea ice is still largely continuous, extending from the North American coast to the Siberian coast interrupted only by relatively narrow leads and small polynyas. Melting of these arctic rivers begins in the headwaters and progresses downstream. The increasing river discharge and snow-melt from surrounding terrain flood the sea ice in coastal areas [Mathews and Stringer, 1984]. These over-ice-floods are referred to as overflows in this report. As spring progresses the

relatively warm and fresh riverine water transports an increasing amount of heat from the terrestrial environment to the marine environment. The flood waters also transport sediments which are deposited on the sea ice, decreasing the sea ice albedo and hence increasing solar absorption.

The Mackenzie River is one of the primary sources of fresh water for the arctic basin supplying about $380 \text{ km}^3 \text{ yr}^{-1}$ [UNESCO, 1988] to the Beaufort Sea and is the largest single source of sediment for the area [Milliman and Meade, 1983]. Mean monthly stream flow ranges from less than $5000 \text{ m}^3 \text{ s}^{-1}$ during winter months to nearly $30\,000 \text{ m}^3 \text{ s}^{-1}$ at peak discharge in June measured at Arctic Red River (Water Survey of Canada, Yellowknife, NWT). The average rise in water level at the time of the spring peak discharge is approximately 5.5 m measured at Inuvik [Marsh and Hey, 1989].

Surface circulation in the Beaufort Sea is dominated by the anticyclonic Beaufort Gyre but an eastward-flowing undercurrent seaward of the 50 m isobath is also present [Aagard, 1984]. On the Mackenzie shelf, water mass structure and boundaries are complex with a variety of temperature, salinity and turbidity fronts that co-exist at any given time [Carmack et al., 1989]. Sources of water on the Mackenzie shelf have been quantified using the distribution of $\delta^{18}\text{O}$, salinity, temperature and nutrients [Macdonald et al., 1989].

The Mackenzie River discharges onto a shallow continental shelf extending 60 to 80 km offshore. Extensive ridging occurs at the shelf break during the winter as the pack ice moves laterally against the nearshore ice in a 'shear zone'. In late winter, an annually recurrent polynya develops here and separates the pack ice from the shorefast ice. The ridged ice in the shear zone creates large-scale under-ice topography (keels) which effectively separates the shelf water from the Arctic Ocean [Macdonald and Carmack, 1991]. Over winter, the Mackenzie River maintains a relatively large discharge ($\approx 3500 \text{ m}^3 \text{ s}^{-1}$). This discharge pools on the nearshore side of the ice-ridge system since it is buoyant compared to the relatively saline shelf water and is effectively dammed by the keels of

the shear ridges. The wintertime discharge is sufficient to maintain a consistent salinity structure on the shelf and replenish the supply of freshwater as the ice is formed. Peak discharge ($\approx 30\,000\text{ m}^3\text{ s}^{-1}$) occurs in early June but doesn't appear to have a significant effect on the shelf salinity profile at this time except near the ridging where a deepening of isohalines occurs as the riverine water flows underneath the hanging-dam structure.

A map of the study region is shown in figure 3.1 with a detailed inset of the Mackenzie River delta. A series of generalized schematic diagrams derived from the visible band satellite images recorded in 1986 (see Dean et al. [1994]) shows the ice breakup process offshore of the Mackenzie River delta (figure 3.2). This schematic highlights the spatial patterns of breakup as they change in time.

3.2.2 Satellite Imagery

Satellite imagery provides a repetitive and synoptic view of marine and terrestrial environments and an instantaneous view of dynamic hydrologic environments. These data also provide quantitative information on surface temperatures and albedo. Data from the Advanced Very High Resolution Radiometer (AVHRR) and Landsat TM sensors were used in this study. The AVHRR data records conditions at least twice daily with a 2200 km swath width at 1 km resolution. Landsat images offer higher resolution but are less frequent in coverage. Data are collected by both platforms in visible, reflected infrared and thermal infrared wavelengths. Dean et al. [1994] provide a comprehensive qualitative analysis of the satellite imagery used in this study.

AVHRR imagery from several years were reviewed to identify the year with the largest number of low cloud-cover images showing river and sea ice interactions. This search revealed 1986 as the year with the most favorable cloud conditions. Interannual analyses of sea ice patterns [Morris, 1993] and river discharge records from the Water Survey

Canada indicate that 1986 is not an unusual year in this respect and thus our results should represent general conditions in this area.

Thirty-one images recorded between 25 May and 16 August were found to have low cloud-cover in the vicinity of the delta and showed the temporal variability of the thaw process. Fifteen of the thirty-one images were selected for digital processing. Only data from the NOAA-9 satellite were purchased for radiometric consistency. Two AVHRR and a Landsat TM digital data set were also acquired in the spring of 1991 to coincide with field observations.

The satellite data were processed to provide quantitative measurements and qualitative interpretations. The AVHRR data were subsectioned, geometrically corrected and radiometrically calibrated using modules in the Land Analysis System (LAS) image processing software. The same modules are used to calculate temperature and albedo using equations and procedures described in technical manuals [Kidwell, K. B., Editor, 1991; Planet, ed., 1988]. Temperature and albedo values can be read from the calibrated thermal and albedo images. These analyses were consistently applied to each image such that inter-image comparisons could be made. Land was masked on these data and a digital coastline was merged with the images to help differentiate land and marine features and for geographic reference.

3.3 Analysis

When developing a climatological ice melt model of this region, it is necessary to determine the main factors contributing to the ice removal process. There are a number of factors to consider although two of these need to be specifically discussed in context to the model development later. These include, 1) the sensible heat supplied to the region through the river discharge and 2) the radiative transfer. Once these are known, then a model using

basic parameters can be developed and run to test the overall sensitivity of the region to changes in critical parameters.

3.3.1 Sensible Heat

Of particular importance to parameterizing the heat supplied to the region is the area immediately offshore from the river delta where, during the initial breakup, ice is flooded (overflows) but soon the ice begins to recede from the coast. The question is asked, 'When do overflow areas become open water?' since the mechanism of ice melt, that is, solar absorption versus sensible heat, is dependent on the answer. Also, does the volume of the overflow account for all or only part of the river discharge? The spatial coverage of the satellite imagery easily provides a quantitative measure of the area of water and a time sequence of this is obtained using the set of images. There is seen on the imagery (or figure 3.2 for example) a recession of water that coincides with the peak of discharge at approximately 4 June. The area of water immediately adjacent to the coast is plotted in figure 3.3. Superimposed on this plot is the discharge (dashed line) for 1986. The thermal images for the first three dates (25 May, 4 June, and 11 June) show the water to be nearly isothermal with the ice cover. Since the water and ice are assumed to be in equilibrium at the melting point and the calculated area of water diminishes after the peak in discharge – presumably draining through cracks and thereby re-exposing ice, it is interpreted that these images are depicting flooded ice. Subsequent areal measurements (14 June, 19 June, and 3 July) diverge from the discharge curve and thermal images during this period show the water adjacent to the coast significantly above the melting point. Thus it is apparent that the ice is now melting laterally away from the coast.

Early in the season, therefore, at least some of the water seen on satellite imagery is flooded ice. However, based on volume calculations using actual 1986 discharge measurements and depths, only a fraction of the water can be contributing to the flooded areas.

Estimating a generous depth of flooded ice at 1 m and using the area measured from the images, only about 10% of the accumulated discharge can be accounted for. Thus, about 90% of the discharge must be flowing underneath the ice cover. This quantity of water, and therefore its heat, flowing underneath the ice led us to suspect that vertical melting due to the sensible heat of the river water is a more significant component of total ice removal than is lateral melting from the shoreline.

3.3.2 Radiative Transfer

Sea ice greatly restricts the absorption of solar energy by underlying water. Thawing of ice exposes the water to the atmosphere thus significantly increasing the absorption of solar energy. In addition, the higher levels of heat and moisture exchanges between the water and the atmosphere may warm the surrounding coastal region and increase precipitation. The authors hypothesize that in coastal regions the area of exposed sea surface and length of the time that the sea surface is exposed to the atmosphere is strongly influenced by rivers.

To assess the effects of exposed water, the heat flux was approximated and compared in areas offshore of the delta, along the coast east and west of the delta (figure 3.4), and far to the east adjacent to Banks Island (see figure 3.1). The approximated heat flux is based on the average albedo values of each area with values derived from the time-sequential, satellite images from visible and near infrared bands. The results are shown as plots of albedo versus time (figure 3.4). The lower curve in each graph is the average albedo of water and ice in the delta region and the upper curve is the average albedo from the surface containing mostly ice in the coastal regions where minimal river discharge occurs. These data show that the average albedo in thawed zones offshore from deltas (lower curve) is lower than other areas along coasts that have little or no river input (upper curve). The integrated area bounded by each curve is proportional to the total absorbed

energy per unit area over the breakup season. Since the solar radiation is assumed to be equal for each site, the difference between these two curves (represented by the shaded region) will be representative of the additional energy gained by the lower-albedo delta region. The integration shows that during the break-up period (May-July) 30% more of the visible wavelength energy and 25% more of the near-infrared wavelength energy is absorbed by the region offshore from the delta compared to coastal areas with minimal river discharge.

3.4 The River-Ice Interaction Model

In this study, we consider only those changes in the nearshore ice due to thermal forcing typical of an arctic spring beginning around late May and continuing to mid-July. An examination of the satellite imagery suggest there is little movement of the shorefast ice during the melt season, therefore, to isolate the thermodynamics of the region, other processes such as advection and internal stresses are ignored. Heat fluxes on the upper and lower horizontal surfaces of the ice cover are treated separately to distinguish between atmospheric heat exchanges and the sensible heat input from the river discharge. The ice cover is assumed to be uniform in thickness, free of snow, and isothermal (or very nearly so) such that heat conduction within the ice is absent or negligible.

3.4.1 The Upper Surface Heat Balance

The governing equation on the upper surface of the ice cover can be written as:

$$\sum F = (1 - i_o)(1 - \alpha)F_r - \epsilon_i \sigma T_o^4 + F_i + F_s + F_l + F_c \quad (3.1)$$

where the six terms on the right-hand side are, respectively, the absorbed shortwave radiation, the outgoing longwave radiation, the incoming longwave flux, the sensible heat

flux, the latent heat flux and conduction. At the onset of spring when solar radiation and air temperatures are increasing, the available energy increases the surface temperature, T_o , to achieve thermal equilibrium with the atmosphere. Once the surface warms to the melting point, any additional energy becomes available for melting ice. The surface heat balance is then represented by the equation

$$\left(\frac{dh}{dt}\right)_{surface} = -\frac{\sum F}{\rho_i L_f}$$

where ρ_i is the ice density (900 kg m^{-3}), L_f the latent heat of fusion and h is the ice thickness in units of meters at time t , in seconds.

The heat fluxes in equation 3.1 are based on the models and parameters of Maykut and Perovich [1987] and the reader is referred to that paper for most of the details. All the terms on the right-hand side of equation 3.1 except for the absorbed shortwave term are parameterized as functions of the surface temperature, T_o (see the appendix for the functional form of the various terms). The incoming shortwave radiation, F_r , is interpolated from the monthly averages given in Maykut and Untersteiner [1971]. Air temperatures for 1986 were obtained at Tuktoyaktuk, NWT, located in the eastern portion of the delta and were smoothed to fit a sine function in the model. The albedo, α is allowed to vary with ice thickness based on the empirical relationship given in Maykut and Untersteiner [1971]. Other variables required in the parameterization of the heat fluxes included cloudiness, wind speed and relative humidity. These were taken from the June average values for the Mackenzie region given in Brower et al. [1988].

One aspect of the parameterization in the treatment of absorbed radiation will be mentioned here. Not all of the incoming shortwave radiation at the surface of the ice is immediately available for melting. Following Maykut and Perovich [1987], a fraction of this energy (represented by $i_o(1 - \alpha)$) is transmitted through the ice layer with an exponential attenuation and absorbed internally. The ice is thus partitioned into a surface layer of 10 cm where the remaining fraction of shortwave energy, $(1 - i_o)(1 - \alpha)F_r$, is

immediately available for melting and a lower layer where the transmitted energy goes toward internal melting rather than direct changes in ice thickness. Internal melting of sea ice increases the brine volume and consequently decreases the amount of energy required for mass changes. This is accounted for in the model by allowing the latent heat of fusion, L_f , to become a time-dependent variable.

3.4.2 The Riverine Heat Flux

The heat supplied by the river discharge to the base of the ice cover is analogous to the oceanic heat flux included in most standard thermodynamic sea ice models. Oceanic heat flux is a poorly understood parameter and its value likely varies in space and time, however, most models assume a constant value between 0 and 10 W m^{-2} . The Maykut and Untersteiner [1971] results show the equilibrium thickness of sea ice to be highly sensitive to this parameter, decreasing from about 6 m to zero for a change in heat flux from 0 to 7 W m^{-2} . Utilizing the sequence of satellite images as well as the general features of the Mackenzie shelf morphology and river discharge, the basal heat supplied to the ice cover will be explicitly parameterized in the development that follows.

As a simple and first approach, the riverine influence is modeled as a convective heat flux analogous to the atmospheric sensible heat at the upper surface of the ice. Convective heat is typically based on the bulk properties of the flow without including specific effects such as friction, velocity, roughness length or the presence of a viscous sublayer for smooth flow. This is achieved by incorporating the various physical processes into a single non-dimensional convective heat-transfer coefficient, C_s . Thus, the riverine heat flux at the base of the ice cover is represented by an equation of the form:

$$F_{river} = f_{int}\rho_w c_p C_s u \Delta T \quad (3.2)$$

where $\Delta T = (T_{plume} - T_{melt})$ is the difference between the bulk river plume temperature and the melting point (here 273 K) and $f_{int} = A_{plume}/A_{ice}$ is the ratio of the areal extent

of the river plume in contact with the ice cover to the total area of the ice. Also in equation 3.2, ρ_w is the density of water (1000 kg m^{-3}), c_p is the specific heat of water ($4200 \text{ J kg}^{-1} \text{ K}^{-1}$), and u is the bulk plume speed in m s^{-1} . Since the base of the ice cover is assumed to be in equilibrium with the shelf water at the melting temperature, all of the river energy is available for bottom ablation, that is,

$$\left(\frac{dh}{dt}\right)_{base} = -\frac{F_{river}}{\rho_i L_f}$$

3.4.3 Discussion of the River Parameters

Excepting ρ_w and c_p , the remaining four terms in equation 3.2: f_{int} , u , ΔT , and C_s are not directly known. These terms are estimated, at least to within an order of magnitude, using geometrical arguments, imagery measurements and timing constraints on the breakup of the shelf ice. To begin estimating these parameters, an idealized geometrical representation of the shelf region will be employed and is shown in figure 3.5. The shelf is represented by a cylindrical section with an inner radius of 30 km, outer radius of 90 km and an angular spread of 90 degrees. Because the fresh and relatively warm discharge is buoyant, the effective shelf depth will be less than the actual shelf depth of about 10 m. Instead, an approximate mixing depth of 2 m is used, based on the salinity profiles and calculations of standing freshwater stock given in Macdonald and Carmack [1991]. In this geometry, the modeled areal coverage is roughly $5 \times 10^9 \text{ m}^2$ with a total volume of $1 \times 10^{10} \text{ m}^3$.

The discharge into the model region cannot be accurately known, since the published Canadian measurements (Water Survey of Canada 10LCO14, 1986) are taken at Arctic Red River far upstream before the Mackenzie River separates into its various channels at the delta. It should be noted, however, that the majority of discharge (approx. 80%) occurs in the western portion of the delta (personal comm., 1993 S. Fafassnacht, Yellowknife, NWT and W. Hanna, Inuvik, Environment of Canada) where, incidentally, melting is ear-

liest and most extensive as is apparent in figure 3.2. With this information, the average discharge into the model region for the breakup period is approximately $2 \times 10^4 \text{ m}^3 \text{ s}^{-1}$.

Without a spatial and temporal series of salinity profiles in the shelf region, it is difficult to estimate the interaction ratio of the under-ice plume to the ice cover, f_{int} . However, this could be approximated by the residence time of the freshwater influx. Assuming the above values for discharge and shelf volume, the residence time for the freshwater in the model space is only 6 days. Since this is far shorter than the roughly 30 day melt period, the interaction dimension, is taken to be unity, that is, the plume is treated as if it were effectively in thermal contact with the entire ice cover as it flows out onto the shelf.

The model shelf dimensions and discharge allow an estimation for the relative speed, u . The cross-sectional area receiving the freshwater input is roughly $9 \times 10^4 \text{ m}^2$ and, assuming the velocity is constant with depth, the discharge enters the region with a speed of $u_o = 0.2 \text{ m s}^{-1}$. Continuity requires this to fall off inversely with distance as it radially spreads over the model region. To avoid using spatially dependent quantities in the model, an averaged value over the shelf region is used resulting in a parameterized bulk plume speed of 0.1 m s^{-1} .

The thermal forcing, ΔT , representing the temperature of the shelf water in contact with the ice cover is derived from the calibrated thermal band AVHRR images. The distinct patches of open water adjacent to the delta establish initial temperature patterns as the river enters the model space. This temperature is seen to progress from near 0°C at the peak of discharge (1 June) to 10°C thirty days later when the delta is largely free of ice. Thus, the thermal forcing is given a temporal dependence as breakup proceeds although, as in the other parameters, a spatial dependency is ignored.

It should be pointed out, however, that the initial temperature adjacent to the coast

should not be used for the thermal forcing. These measurements are taken before the river enters the region and mixes with the shelf water. Thus, the sensible heat will be overestimated if these temperatures are used in the thermal forcing. To account for this, mixing of the river discharge and shelf water is allowed with a specified ratio. The discharge represents a daily standing stock of freshwater of 0.25 m when spread over the model region. If it is assumed, as previously, this mixes to a depth of 2 m, the ratio is then 1/8. Thus, as the initial river temperature linearly increases over time at a rate of 10 K per 30 days, it is cumulatively mixed with seven parts of shelf water at its previous temperature. This results in an exponential-like increase over time in the shelf water's temperature, although simply stated, the modeled effect is to reduce the thermal forcing rate to about half the river's warming rate, that is 5 K per 30 days. We also assume that the cooling of the plume by melting the ice is small – likely much smaller than the 're-charge' of temperature from riverine input and mixing.

The last term to discuss is the heat transfer coefficient, C_s . Typically, given a melt rate, dh/dt , one arrives at this coefficient by measuring the bulk flow parameters u and ΔT and reversing equation 3.2 to solve for C_s . This method eliminates the need to estimate the heat flux from turbulent temperature and velocity fluctuations or from the mean temperature and velocity profiles. Josberger [1987] presented such measurements from the 1983 Marginal Ice Zone Experiments (MIZEX) in the Bering Sea and Fram Strait by measuring the bottom ablation of ice floes advected into regions where they encountered higher relative ice-water speeds and ocean temperatures. His reported values of C_s showed little variation over a wide range of measured melt rates, relative ice-water speeds and seawater temperature as well as for the two different sites. These values ranged from 2×10^{-4} to 8×10^{-4} and were even narrower (2 to 5 ($\times 10^{-4}$)) for the Fram Strait measurements. One reason for the smaller range in the Fram Strait floes was attributed to a smoother ice pack than the Bering Sea ice. Increased fracturing and rafting creates a rougher surface and enhances turbulent transfer of heat to the ice causing the wider

range of values. The ice floes studied in the Fram Strait had horizontal dimensions of approximately 80 m and were exposed to relative ice-water speeds at the 2 m depth from 0.1 to 0.2 m s⁻¹ and a thermal forcing of 2 to 5 K. Since the nearshore ice in the Mackenzie River delta is relatively smooth and parameters estimated in the delta are very similar to those measured in the Fram Strait, this makes comparisons to the Fram Strait data more useful. As will be shown in the next section, a value of $C_s = 1 \times 10^{-4}$ gives the best results for the Mackenzie River delta ice.

3.5 Results and Conclusions

Equation 3.1 is a fourth-order polynomial in the surface temperature, T_o (see the appendix) and represents the energy gained at the top surface of the ice. At each time step the four (complex) roots of T_o are found and a physically realistic solution is sought whereupon T_o is updated until such a time that it reaches the melting temperature. At this point, energy gained at the surface becomes available for melting and the surface temperature is maintained at 273 K. The surface forcing terms all vary slowly over time and hence place no real constraints on the time step, dt . However, surface melting is assumed to take place in a layer 10 cm thick which requires the time step to be small enough such that a change in ice thickness greater than 10 cm does not occur over any one step. Here, an Euler scheme is employed with a time step of 0.5 days, although there are no diurnal variations in any of the forcing terms.

Numerical simulations of the spring breakup period from 25 May (day 145) through mid-July were run with no basal heat flux as a control case representing regions without river discharge. The equilibrium surface temperature on 25 May started at 269 K and did not reach the melting point until 3 June (day 154). Complete removal of the ice cover occurred on 6 July (day 187), requiring a total energy input of 5.4×10^8 J m⁻². The net

atmospheric heat flux at the upper surface is shown in figure 3.6 along with its various components. The ice decays in parabolic form in response to this nearly linear increase in the net surface flux.

Comparisons of ice decay for the control case were made to the Sachs Harbor, NWT data given by Bilello [1980] where there is no river discharge. The average decay envelope for a 16 year period here indicates that the onset of melt occurs about 25 May and the coastal ice is completely removed around 10 July. An empirical relationship was derived for the data relating the period of decay to the accumulated thawing degree-days obtained by summing the daily difference between positive mean air temperatures and the melting temperature. For the present study, we use this empirical relationship with 1986 air temperatures at Tuktoyaktuk. This predicted complete removal of the ice cover by day 190, in good agreement with the numerical simulation result of day 187 (see figure 3.7, dashed line). Since the empirical relationship is based on air temperatures, this also emphasizes the importance of the sensible heat flux in the surface balance of coastal regions.

Next, numerical simulations were run for the case with river input where the thermal forcing in equation 3.2 was 'turned on' on 1 June (day 151) at the peak of discharge. Several cases were run allowing the heat transfer coefficient to assume values between 0.25×10^{-4} and 4×10^{-4} . The ice decay curves for these simulations are plotted as solid lines in figure 3.7 and, for comparison, the decay curve without river discharge representing the limiting case is shown as a dashed line. The results of these simulations were compared to the date of breakup derived from the 1986 sequence of images. The images show that all of the fast ice broke into small floes by 29 June (day 180) and were completely gone by the next image scene on 3 July (day 184). This requires a heat transfer coefficient of $C_s = 1 \times 10^{-4}$. The basal heat flux calculated with this coefficient is shown along with the net atmospheric heat flux in figure 3.8. Integrating these two curves gives the relative contribution from each energy source resulting in 58% atmospheric and 42% river heat

required to melt the nearshore ice.

In parameterizing the various river terms, no errors associated with them are given since most of the arguments are first order determinations necessitated by the available data. Sensitivity to changes in the magnitude of any of the river parameters such as the heat transfer coefficient C_s , the bulk plume speed u , the fractional plume coverage f_{int} or the thermal forcing ΔT is suggested by the family of curves in figure 3.7. Since the river heat flux (equation 3.2) responds linearly to these terms, a single change to any one of them will have the same result on the energy supplied by the river and the date of breakup. For instance, an increase in any one parameter by a factor of two results in breakup about four days earlier. The fraction of energy supplied by the river as a function of changes to one of these terms (for example, C_s) is shown in figure 3.9 where a non-linear dependence is apparent.

A different sensitivity occurs as a result of the initial date the thermal forcing ΔT is 'turned on'. Since the warming rate of the river water is linear, changing the starting date results in proportional changes to the amount of energy supplied by the river over the breakup period. Here, an earlier warming of the river by one week removes the ice cover approximately three days earlier as shown in figure 3.10. The resulting fraction of energy supplied by the river in this case is plotted in figure 3.11 where a linear dependence is apparent.

Finally, the modeling approach taken here is necessarily simplistic given the nature of the problem and the lack of quantitative data in the water column. Spatial variability and a realistic mixed layer model for the shelf water was ignored. Because this was a sensitivity test, only climatological values for solar and atmospheric forcing were used. Also, only the spring melt period has been addressed in the present investigation. However, this approach highlights the key elements regarding the influence of river discharge on sea ice. Rivers do indeed supply a significant amount of sensible heat, accounting in this case for

approximately half of the energy required to melt the ice in the nearshore region. As a result, coastal areas receiving river discharge are free of ice conditions 7 to 14 days earlier. This occurs at a time when increasing air temperatures and solar radiation are available for the region's overall heat balance and it is not clear what importance this has on the local climate. Future studies should include an annual energy balance and model in a similar fashion the open-water and ice-growth seasons as well as occasion-specific values for meteorological and solar forcing. Such a model could then investigate the feedback mechanisms related to a longer open-water season and assess the sensitivity of the region to possible climatic change.

Appendix

For the sake of brevity, many of the functional forms of the various terms in equation 3.1 were omitted in the text. These are presented here for completeness, see also Maykut and Perovich [1987]. The right-hand side of equation 3.1 requires the following terms:

Parameter:	Term:	Formulation:
Absorbed Shortwave	$(1 - i_o)(1 - \alpha)F_r$	empirical data
Outgoing Longwave	$-\epsilon_i \sigma T_o^4$	Stefan-Boltzmann law
Incoming Longwave	F_i	$(0.7855 + 0.223Cl^{2.75})\sigma T_o^4$
Sensible Heat	F_s	$\rho_a c_{ap} C_{as} u_a (T_a - T_o)$
Latent Heat	F_l	$(0.622\rho_a L_v C_e / p_o) u_a (r e_{as} - e_{is})$

where Cl is cloudiness, C_e and C_{as} are bulk convective heat transfer coefficients, p_o is atmospheric pressure, r is relative humidity and e is partial pressure of water vapor. In general, parameters with subscript a are atmospheric terms. Thus, the explicit form of the fourth order equation is:

$$\sum F = (1 - i_o)(1 - \alpha)F_r - \epsilon_i \sigma T_o^4 + (0.7855 + 0.223Cl^{2.75})\sigma T_o^4 +$$

$$\rho_a c_{ap} C_{as} u_a (T_a - T_o) + (0.622 \rho_a L_v C_e / p_o) u_a (r e_{as} - e_{is})$$

The latent heat, L_f varied with time to allow for increased brine volume due to internal melting as radiation is transmitted and absorbed into the lower layer of the ice cover. This assumes the form:

$$\frac{dL_f}{dt} = \frac{i_o(1 - \alpha)(1 - e^{\kappa(h-h_o)})f_r}{\rho_i h}$$

where $\kappa = 1.5 \text{ m}^{-1}$ is the bulk extinction coefficient for the transmitted solar radiation and h_o is the thickness of the surface layer (here 10 cm) which absorbs the shortwave radiation.

Acknowledgments

The authors would like to thank the Polar Continental Shelf Project for providing accommodations and helicopter support, and the Water Survey of Canada, Inuvik for providing ice drilling equipment. We thank the Water Survey of Canada, Yellowknife for providing river discharge records and other very cordial assistance. Dr. Tom Weingartner organized and participated in the collection of field data. Tom George provided aircraft support and assistance in aerial photography and video. Image processing was performed by Kristina Ahlnaes using the Interactive Image Analysis System at the Alaska SAR Facility and the University of Alaska, Alaska Data Visualization and Analysis Laboratory. This project was funded by NASA grant NAGW 1835.

References

- Aagard, K. (1984). The beaufort undercurrent, in the alaska beaufort sea: Ecosystems and environments. pp. 47-71. San Diego, Calif.: Academic.

- Aagard, K. and L. Coachman (1975). Toward an ice-free Arctic Ocean. *EOS* 56, 484-486.
- Bilello, M. (1980). Decay patterns of fast sea ice in Canada and Alaska. In R. Pritchard (Ed.), *Sea Ice Processes and Models, Proc. of the AIDJEX International Commission on Snow and Ice Symposium*.
- Brower, W., R. Baldwin, C. Williams, J. Wise, and L. Leslie (1988). *Climatic Atlas of the Outer Continental Shelf Waters and the Coastal Regions of Alaska, Vol III, Chukchi and Beaufort Seas*. Department of Defense Document, NAVAIR 50-1C-553.
- Carmack, E. C., R. Macdonald, and J. E. Papadakis (1989). Water mass structure and boundaries in the mackenzie shelf estuary. *J. Geophys. Res.* 94(C12), 18,043-18,055.
- Dean, K., W. Stringer, K. Ahlnaes, S. Searcy, and T. Weingartner (1994). The influence of river discharge on the thawing of sea ice: Mackenzie River Delta: albedo and temperature analysis. *Polar Res.* 13, 83-94.
- Josberger, E. (1987). Bottom ablation and heat transfer coefficients from the 1983 Marginal Ice Zone Experiments. *J. Geophys. Res.* 92(C7), 7012-7016.
- Kidwell, ed., K. B. (1991). *NOAA Polar User Guide (TIROS-N, NOAA 6, NOAA 7, NOAA 8, NOAA 9, NOAA 10, NOAA 11, and NOAA 12)*. National Climatic Data Center, Satellite Data Services Division, Princeton Executive Square, Rm. 100, Washington DC. 20233: National Oceanic and Atmospheric Administration, National Environmental Satellite, Data, and Information Service.
- Macdonald, R. and E. Carmack (1991). The role of large-scale under-ice topography in separating estuary and ocean on an Arctic shelf. *Atmos.-Ocn.* 29(1), 37-53.
- Macdonald, R. W., E. C. Carmack, F. A. McLaughlin, K. Iseki, and D. M. Macdonald (1989). Composition and modification of water masses in the mackenzie shelf estuary. *J. Geophys. Res.* 94(C12), 18,057-18,070.
- Marsh, P. and M. Hey (1989). The flooding hydrology of mackenzie delta lakes near inuvik, n. w. t., canada. *Arctic* 42(1), 41-49.

- Mathews, J. B. and W. J. Stringer (1984). Spring breakup and flushing of an arctic estuary. *J. Geophys. Res.* 89(C2), 2,037–2,079.
- Maykut, G. and D. Perovich (1987). The role of shortwave radiation in the summer decay of a sea ice cover. *J. Geophys. Res.* 92(C7), 7032–7044.
- Maykut, G. and N. Untersteiner (1971). Some results from a time dependent, thermodynamic model of sea ice. *J. Geophys. Res.* 76, 1550–1575.
- Micklin, P. (1981). A preliminary systems analysis of proposed Soviet river diversions on Arctic sea ice. *EOS* 62(19), 489.
- Milliman, J. D. and R. H. Meade (1983). World-wide delivery of sediments to the oceans. *J. Geol.* 91, 1–21.
- Morris, K. (1993). Annually recurring sea ice patterns in the nearshore region of the eastern beaufort sea as determined from satellite data (1974-1986). Master's thesis, Univer. of Alaska Fairbanks.
- Planet, ed., W. G. (1988). *Data Extraction and Calibration of TIROS-N/NOAA Radiometers* (NOAA Tech. Memo. NESS 107 - Rev. 1 ed.). Princeton Executive Square, Rm. 100, Washington DC. 20233: National Climatic Data Center, Satellite Data Services Division.
- Semtner Jr., A. (1984). The climatic response of the Arctic Ocean to Soviet river diversions. *Clim. Change* 6, 109–130.
- UNESCO (1988). World water balance and water resources of the earth. *Stud. and Rep. in Hydrol.* 25.

Figures

3.1	Map of the study region	31
3.2	Schematic diagram of the 1986 visible band AVHRR images	32
3.3	Comparison of the river discharge to areal measurements.....	33
3.4	Average albedo measurements.....	34
3.5	Schematic diagram of the idealized model region.....	35
3.6	Atmospheric heat fluxes	36
3.7	Ice decay curves	37
3.8	A comparison of the net heat flux	38
3.9	The fraction of the total energy supplied by the river	39
3.10	The influence of river melting start date on the ice decay	40
3.11	The fraction of the total energy supplied by the river by start date.....	41

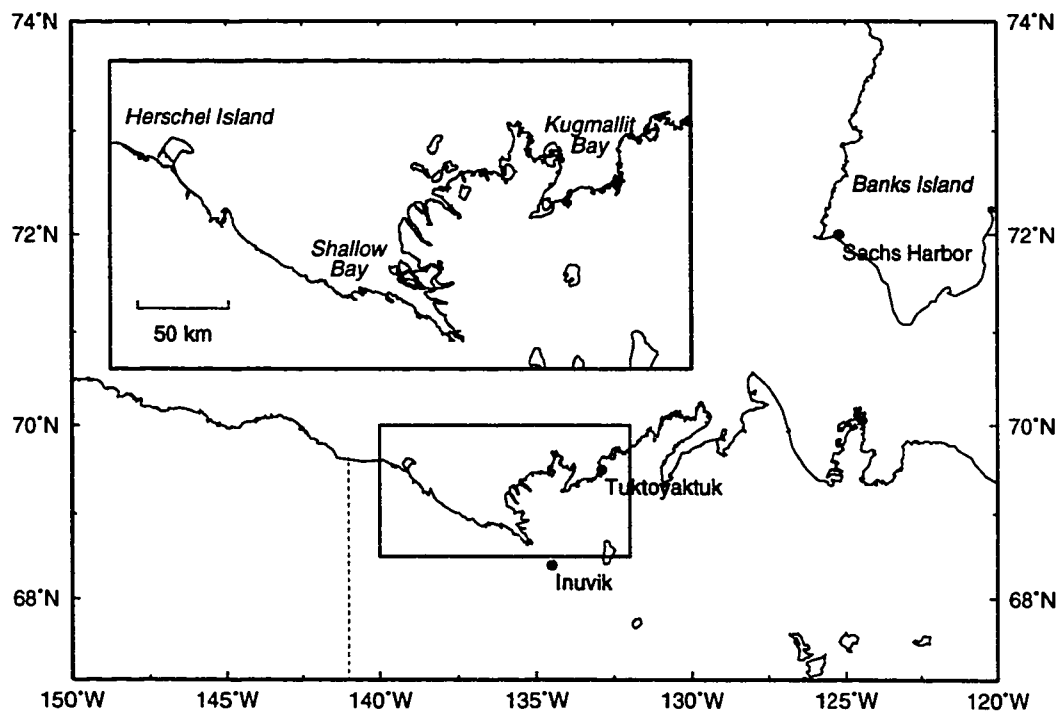


Figure 3.1 Map of the study region including a detailed inset of the Mackenzie River delta

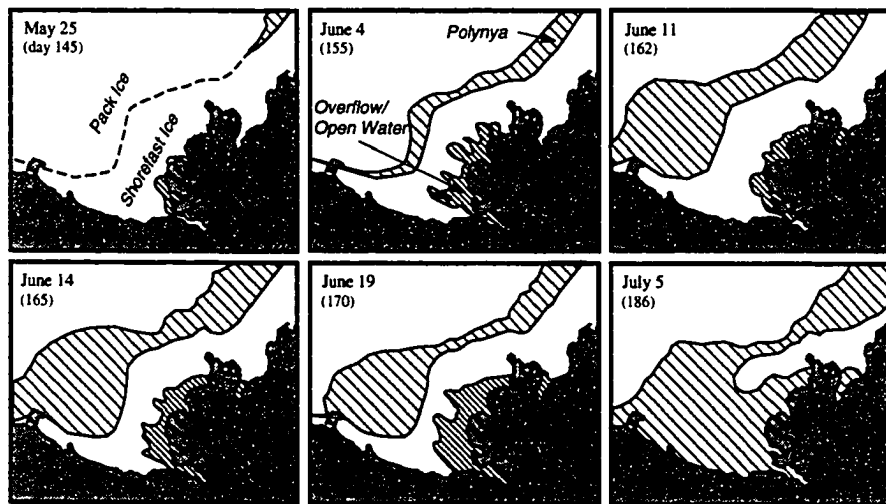


Figure 3.2 Schematic diagram of the 1986 visible band AVHRR images depicting the spring breakup season of the Mackenzie River delta. This sequence also depicts the development of the polynya system separating the shorefast ice from the pack ice.

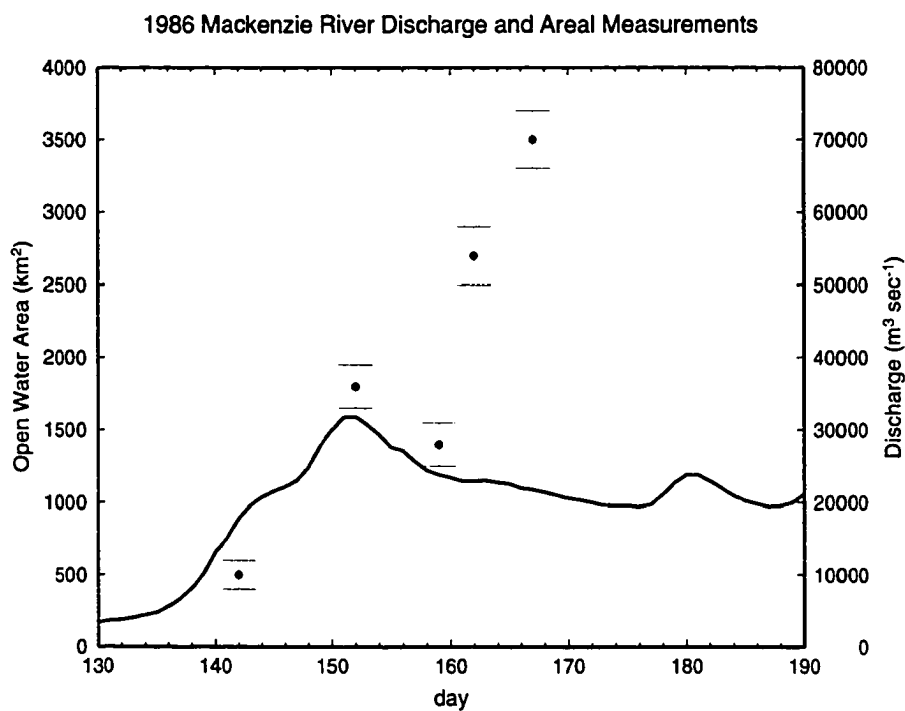


Figure 3.3 Comparison of the 1986 Mackenzie River discharge to areal measurements of the river-induced open water. The dashed line is the discharge curve ($\text{m}^3 \text{s}^{-1}$) while the data points are a calculation of the overflow or open water areas (km^2) immediately adjacent to the coast. The area of open water is derived from the digitally processed AVHRR satellite images. The first three data points follow the temporal discharge pattern and represent overflows on top of the ice cover while later points temporally diverge from the discharge as the area of open water enlarges due to the recession of the ice cover from the coastline.

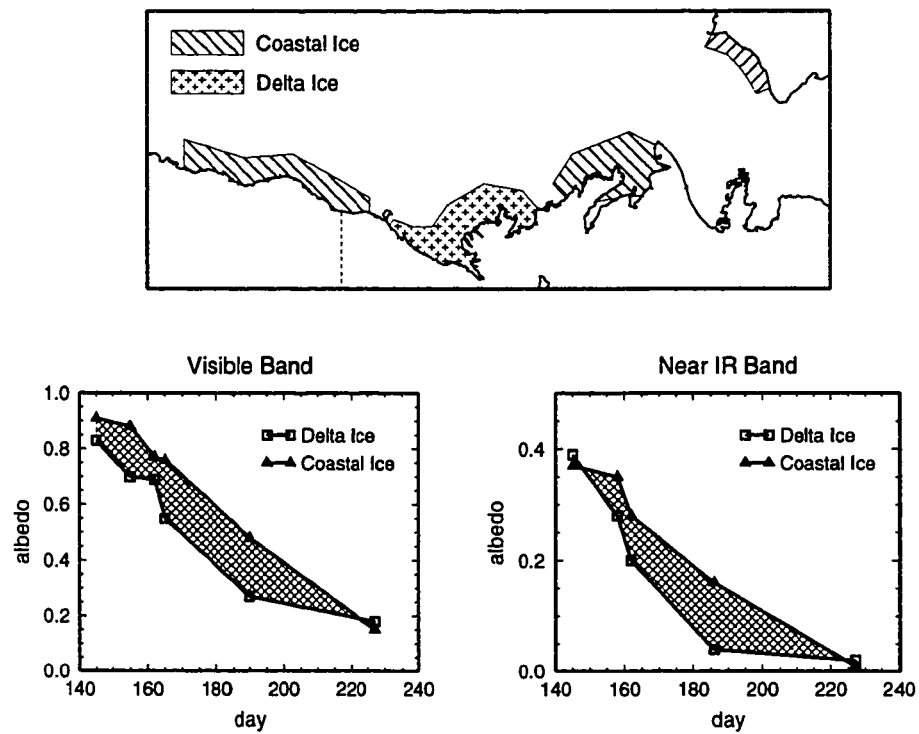


Figure 3.4 Average albedo measurements for the regions shown in the schematic (upper figure) for the visible (lower left) and near infrared (lower right) bands. The delta ice region is consistently lower in albedo and hence absorbs more short-wave radiation than other coastal areas.

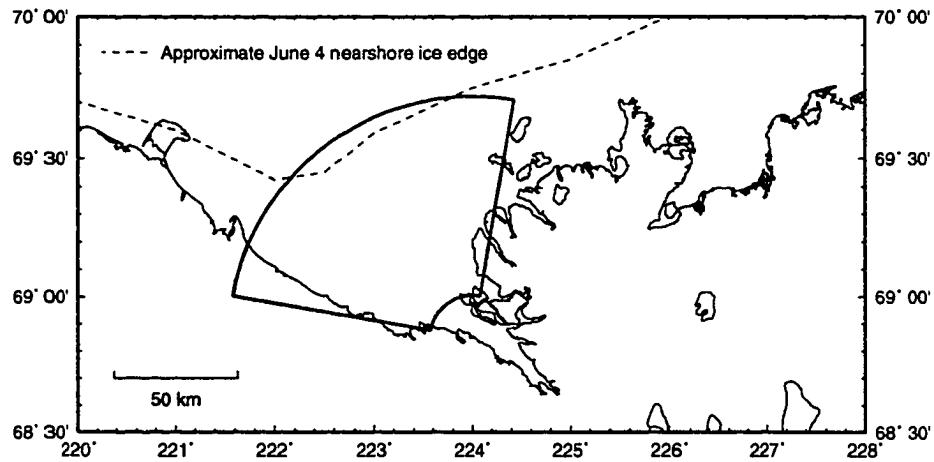


Figure 3.5 Schematic diagram of the idealized model region. Only the western portion of the delta is used for areal calculations since these channels receive the majority of river discharge. The bold cylindrical section has an inner radius of 30 km, an outer radius of 90 km, and an angular spread of 90 degrees.

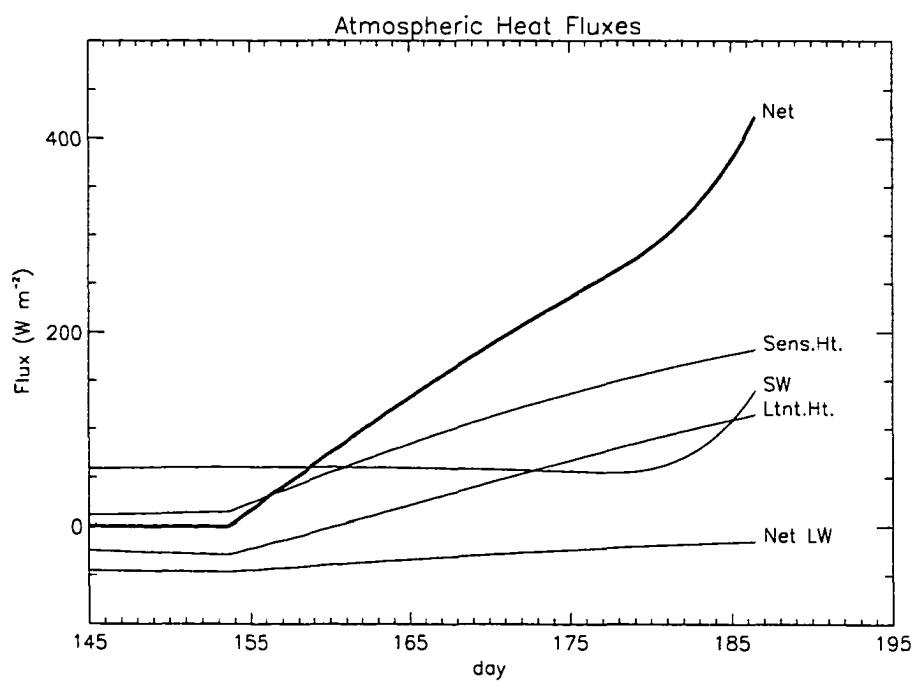


Figure 3.6 Atmospheric heat fluxes show the forcing on the upper surface of the ice cover during the breakup period. Represented are the sensible heat, the absorbed shortwave radiation, the latent heat and the net longwave flux. The net atmospheric flux is shown as a bold line.

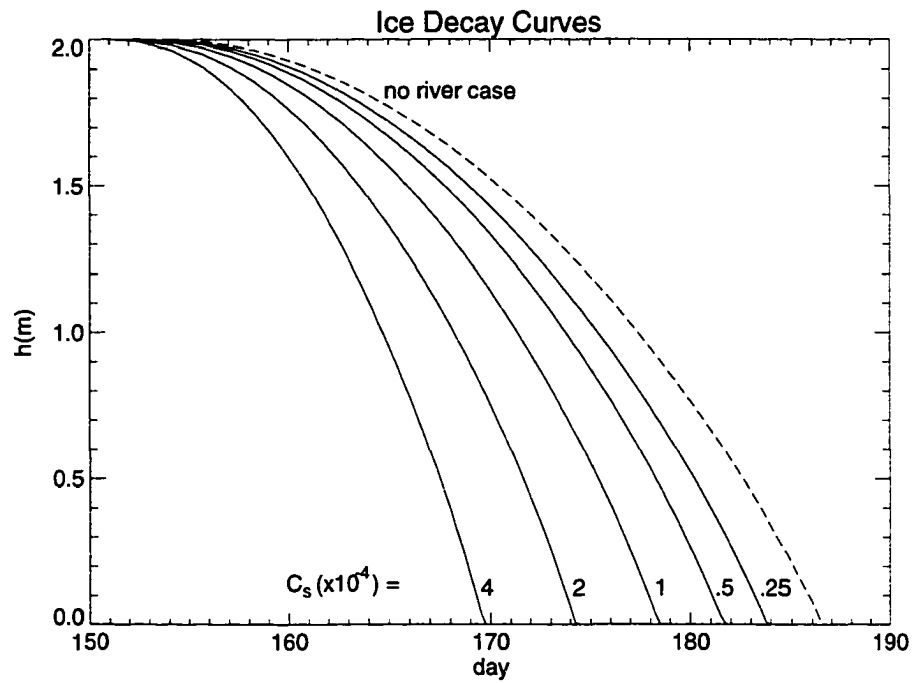


Figure 3.7 Ice decay curves depict the simulated results of melting due to atmospheric forcing and thermal river input. The dashed line is the limiting case where no river heat is applied to the base of the ice cover while the solid curves result from varying the river's heat transfer coefficient term, C_s , from 0.25×10^{-4} to 4.0×10^{-4} .

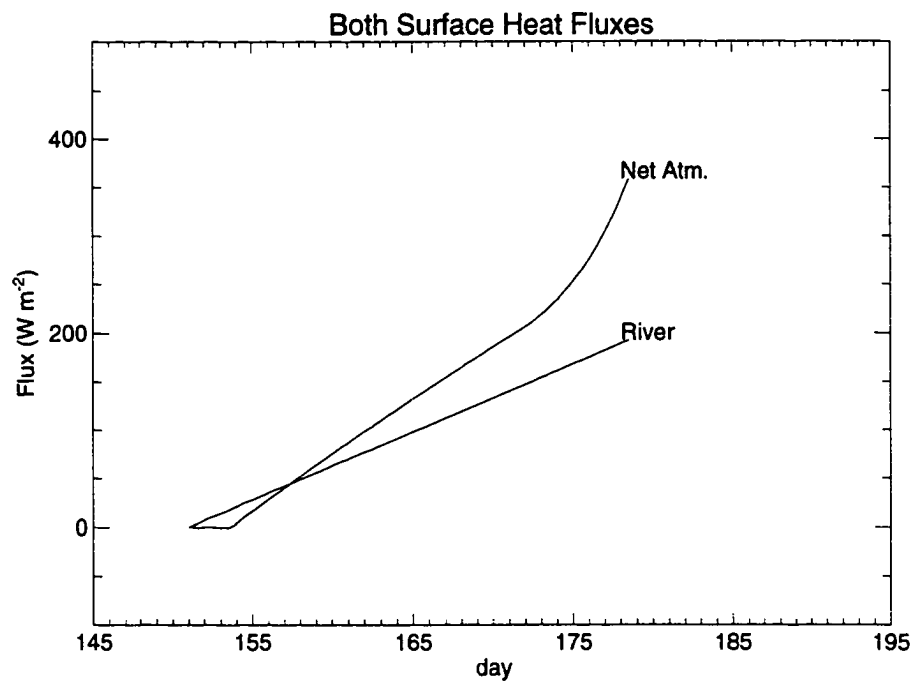


Figure 3.8 A comparison of the net heat flux on both the upper and lower surfaces of the ice cover. The net atmospheric flux is from figure 3.6 while the river flux corresponds to a heat transfer coefficient of $C_s = 1 \times 10^{-4}$. Integrating these curves gives the relative contribution to melting from each source with the result here of 58% atmospheric and 42% river melting.

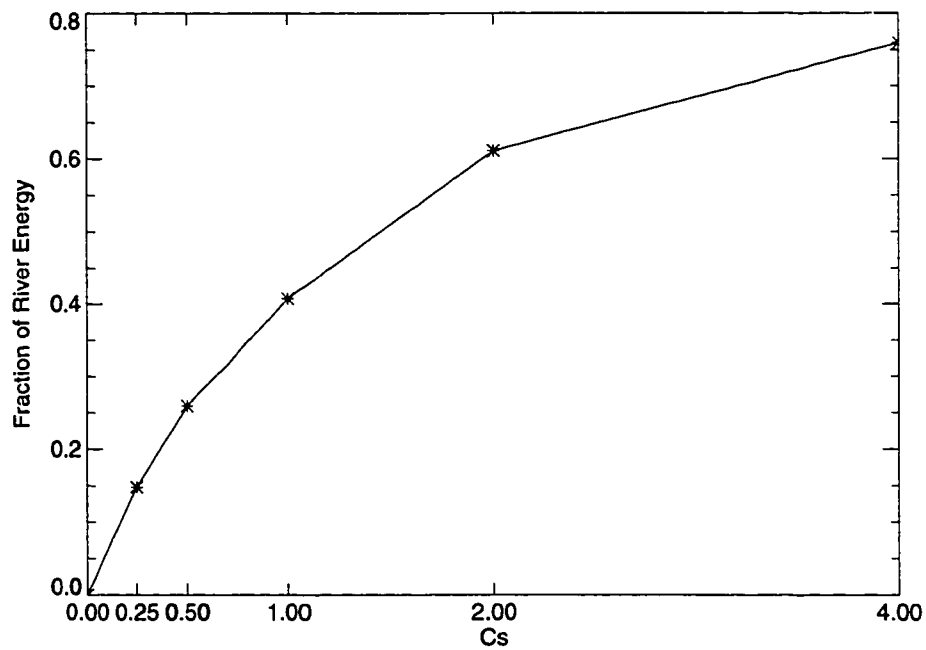


Figure 3.9 The fraction of the total energy supplied by the river in melting the ice cover as a function of the heat transfer coefficient, C_s . The effect on the energy partition is non-linear and, since the river parameterization in the model responds proportionally to all of the terms (u , f_{int} , ΔT), a similar change to any single parameter will have the same net effect on the energy partition.

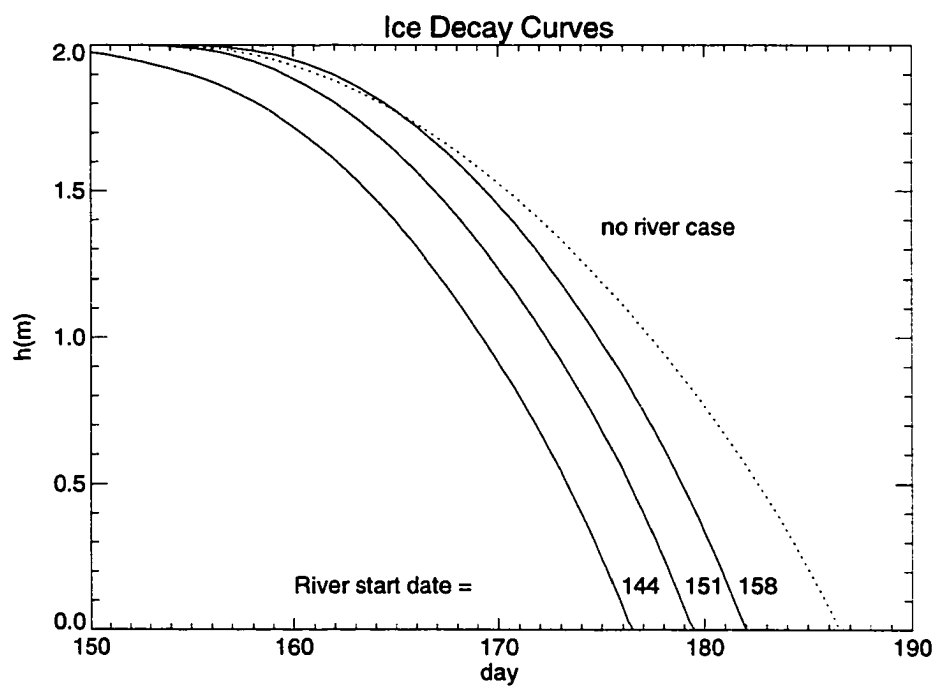


Figure 3.10 The influence of river melting on the ice decay as a result of variations in the date the river heat is first applied. The most typical date is day 151 with a heat transfer coefficient of $C_s = 1 \times 10^{-4}$.

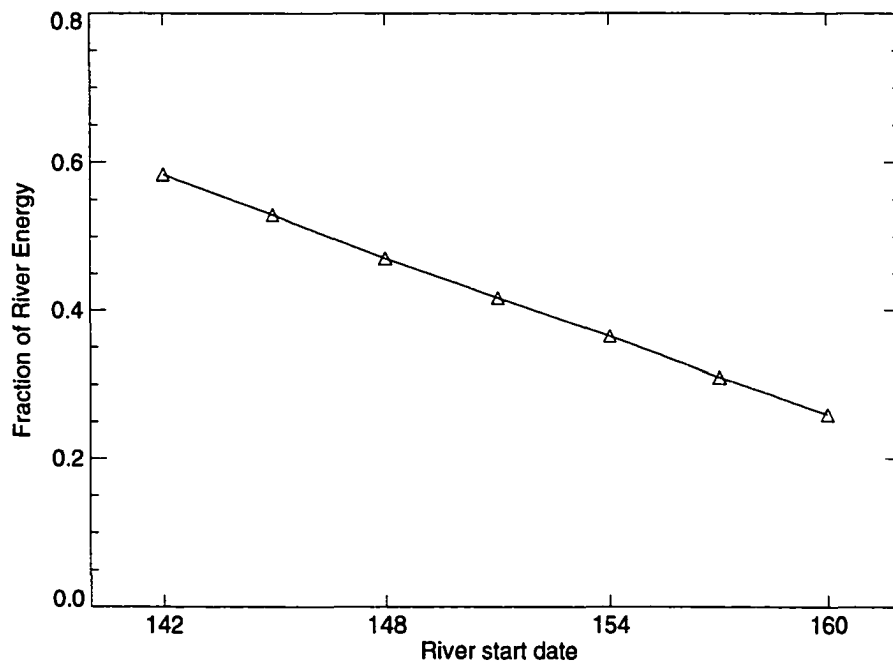


Figure 3.11 The fraction of the total energy supplied by the river in melting the ice cover as a function of the date the river heat is first applied. Note that the effect here is linear.

Chapter 4

PUFF: A high resolution volcanic ash tracking model¹

Abstract

This paper presents a volcanic ash tracking model referred to as PUFF. The model was developed to simulate the movement of airborne ash in near real-time following an eruption for the purposes of hazard warning. The model tracks particles through a Lagrangian formulation of advection, fallout and turbulent diffusion using a random-walk technique. Three recent eruption events are simulated using archived data. AVHRR images from these events are used for comparison and to validate model results.

¹submitted as: Searcy, C., K. Dean, and W. Stringer, *Journal of Volcanology and Geothermal Research*, May 1996

4.1 Introduction

Volcanic eruptions and associated ash clouds are a natural hazard of concern throughout the world. Monitoring techniques include ground-based geophysical instruments, such as seismometers and lightning detection devices as well as visual observing systems, such as satellite imagery, video images and field or pilot reports. Alone, these techniques provide vital but limited information. Seismometers indicate seismic activity associated with an eruption but tell nothing about airborne particles. Visual systems tell us about airborne particles but tell nothing about internal volcanic activity. Also, visual information can be severely limited by weather and daylight or cannot always clearly distinguish airborne ash from meteorological clouds.

In the North Pacific region, eruptions are a serious problem because of the many active volcanos located near major population centers and heavily used air traffic routes. The high frequency of eruptions here (about one per month) with durations ranging from hours to a year constantly threaten the region. The area is vast and remote making it difficult to monitor volcanos, detect eruptions and issue warnings of potential ash hazards. This region is shown in figure 4.1 along with the Anchorage North Pacific (NORPAC) air traffic region and several recently active volcanos.

The Alaska Volcano Observatory (AVO) and the National Weather Service (NWS) monitor and assess volcanos and eruptions in this region. Eruption clouds are tracked with lightning detection devices, satellite images and observers. These tracking systems are limited by location of both instruments and observers, as well as weather and timing of satellite passes. As an aid to these monitoring techniques, an ash tracking model has been developed for predicting ash movement. These forecasts provide information on the location and extent of the ash cloud when observations are not available. Results are also

used to alert concerned parties in near-real time of potential ash cloud location less than an hour after an eruption.

The model, referred to as PUFF, is mainly concerned with the tracking of young eruption clouds. Young eruption clouds are roughly defined here as those that are less than 48 hours old. Young eruption clouds are especially dangerous to aircraft and equipment and cause acute health problems for the following reasons:

- 1) Young eruption clouds contain the highest concentrations and “largest” particles during the duration of that cloud and hence represent the most potentially dangerous period.
- 2) Aircraft that fly over volcanic regions are susceptible to encounters with young eruption clouds, often traveling towards or near a volcano during the eruption without knowledge of the state of the ash cloud because the cloud may have yet to be reported.
- 3) There has never been a lethal encounter by an aircraft (engine power loss) with airborne ash more than 24 hours old (and possibly no more than 12 to 15 hours old [memo from Dr. R. E. Machol, FAA Chief Scientist, 6/11/93, summarizing results from the “Old Volcanic Ash” workshop]).
- 4) Cities, villages and dwellings located within a few hundred kilometers of active volcanos experience the most devastating effects due to by young eruption clouds.

Thus, areas located within a few hundred of kilometers of volcanos are highly susceptible to the effects of young eruption clouds. Most cities and air traffic routes in

the Circum-Pacific region and Alaska fall within this zone. These young eruption clouds severely disrupt air traffic in the region which includes some of the heaviest traffic in the world, mostly in the form of cargo flights. There is a great potential for loss of life, equipment, productivity and commerce during an eruption in this region.

The 1989-1990 eruptions of Redoubt Volcano, Alaska (Dean et al., 1994a; Dean et al., 1994b; Casadevall, 1994) serve as an example of this impact. These eruptions caused extensive disruption of social and economic activity, significant property damage and threatened major loss of human life. In all, this eruption was estimated to cost \$160 million [Tuck and Huskey, 1992]. The aviation industry suffered the most from this event (\$100 million), incurring interruptions of passenger and freight schedules and serious equipment damage. Oil production in Cook Inlet was likewise disrupted and transportation facilities were threatened resulting in sizable costs (\$50 million) to the State and industry.

4.2 Model Background

PUFF is a dynamic pollutant tracer model developed to simulate the behavior of young ash clouds. Initially a research tool, the model has been developed into a reliable interactive software package, offering a number of options with default values and prompting for user-input. As software, it is intended for use in an emergency response situation during an eruption to quickly forecast the position of the ash cloud over some time interval in the immediate future. In this application, it requires near real-time forecast wind data to predict the movement of the ash cloud.

The model, originally developed by H. L. Tanaka [Tanaka, 1991], is based on the three-dimensional Lagrangian formulation of pollutant dispersion. PUFF initializes a col-

lection of discrete ash particles representing a sample of the eruption cloud and calculates transport, turbulent dispersion and fallout for each particle. In Lagrangian form, given a time step Δt , the position vector for each particle is updated from time t to time $(t + \Delta t)$ by the equation:

$$\mathbf{R}_i(t + \Delta t) = \mathbf{R}_i(t) + \mathbf{W}(t)\Delta t + \mathbf{Z}(t)\Delta t + \mathbf{S}_i(t)\Delta t \quad (4.1)$$

where $\mathbf{R}_i(t)$ is the position vector of the i^{th} ash particle at time t , \mathbf{W} is the local wind velocity, \mathbf{Z} is a vector representing turbulent dispersion and \mathbf{S}_i is the terminal gravitational fallout vector, dependent on the i^{th} particle's size. The particles are driven by sampling wind from a four-dimensional mesoscale model and including a random walk formulation for simulating turbulent behavior.

Lagrangian random walk formulations have been used successfully in a variety of applications [Etling et al., 1986; Kao and Yamada, 1988; Physick and Abbs, 1991]. Other numerical techniques used to model ash transport such as the VAFTAD model [Heffter and Stunder, 1993] employ a gridded Eulerian formulation. These techniques calculate mass concentrations for a three-dimensional grid cell at each time step. Grid cells are defined by the driving wind data, which typically are on 6 hour time increments. While this method has proven accurate and reliable, it suffers from the low time and spatial resolution of gridded wind data, prohibiting tracking an ash cloud over a short time or region such as the scale of Cook Inlet (see figure 4.1). Subsampling wind data in a Lagrangian formulation, such as in the PUFF model, allows a higher resolution for tracking ash clouds during the first critical few hours. The Lagrangian method also requires no estimate of the mass distribution of the cloud which would not be available in real-time during an eruption emergency.

4.2.1 Wind Data and Transport

Wind transport, or advection, is calculated for each particle by interpolating four-dimensional wind data to the particle's position and time and transporting it to a new position at the next time step through $\mathbf{W}(t)$ in equation 4.1. Four-dimensional wind fields are derived from forecast meteorological data generated by the National Meteorological Center (NMC) twice-daily forecast runs. This data is available in a variety of formats and from differing forecast models [Peterson and Stackpole, 1989].

The default data set used in PUFF is the Unidata grid model 77, a product available through the University Corporation for Atmospheric Research (UCAR). This is a global data set on a 5° by 2.5° longitude/latitude grid, with 10 standard millibar levels from 1000 mb (surface) to 100 mb (approximately 16 km) in the vertical dimension and a 60 hour forecast in six hour time intervals.

In addition, PUFF currently allows input from the NMC 'regional run' using the Nested Grid Model (NGM; 90 km grid, 48 hour forecast, Alaska region grid 207N) and the 'medium-range run' using the Aviation model (AVN; 190 or 380 km grid, up to 72 hour forecast, Alaska region grid 203J). These data must first be mapped to a longitude/latitude grid and packed to four dimensions as in the Unidata format. This conversion is done while maintaining their inherent spatial and temporal resolution. In fact, any data set at any grid resolution which can be mapped and suitably packed into a 4D *longitude/latitude/height/time* grid is acceptable as input for PUFF.

The advection term (wind) in equation 4.1 accounts for the bulk of each particle's motion, and as such, PUFF essentially computes simple trajectories for each ash particle. In a simulation, each particle independently samples the 4D wind field at its position and time and integrates its motion as the simulation proceeds. PUFF has options for inter-

polating the gridded wind field using a nearest-neighbor scheme or by a 4D cubic-spline technique. In practice, for winds that are slowly varying, nearest-neighbor is sufficiently accurate and significantly reduces the computing time, usually by an order of magnitude or more. Sensitivity studies of similar trajectory models [Rolph and Draxler, 1990] have shown horizontal deviations from 5–25% of the travel distance at 96 hours travel time, with minimal deviations at 24 hours and increasing linearly beyond that. These results were dependent on temporal and spatial grid resolutions and suggested that deviations are not particularly sensitive to cyclonic or anticyclonic conditions.

4.2.2 Turbulent Dispersion

In a real atmosphere where turbulent flow is present, particles tend to disperse with time due to small-scale fluctuations in the field. Since gridded mean wind data cannot resolve these smaller scale turbulent eddies, a numerical technique must be employed to simulate particle dispersion. For this computation, PUFF uses an approximation of pollutant turbulent mixing described by a stochastic process. In a Lagrangian framework, this is realized by superimposing a random walk for each particle on the wind transport term. This motion is described by Z , the second term in equation 4.1. This is a vector containing three-component gaussian random numbers with zero mean and a standard deviation (c_h, c_h, c_v) which is related to the “speed”, or rate, of diffusion (discussed in the following development). The subscripts h and v denote the horizontal and vertical components, respectively. For simplicity, however, the following discussion will assume a one-dimensional case.

A random walk, or Brownian motion, is a process where a particle takes a step at discrete time intervals in such a manner that each step is independent of the others and the variable $z(t)\Delta t = r(t + \Delta t) - r(t)$ is a gaussian variable with zero mean and standard

deviation c . This property of Brownian motion results in the probability density at some point (x, t) given by:

$$q(x, t) = \frac{1}{\sqrt{\pi t}} \exp\left(-\frac{x^2}{2\sigma t}\right) \quad (4.2)$$

with $\sigma = c\sqrt{t\Delta t}$. This is identical to the Green's function solution to the diffusion equation:

$$\frac{\partial q}{\partial t} = \frac{\sigma}{2} \frac{\partial^2 q}{\partial x^2} \quad (4.3)$$

with a point source for initial data $q(x, 0) = \delta(x)$ (δ = Dirac delta). In other words, if one allows particles to leave the origin in the (x, t) plane and wander about by Brownian motion, the density of these particles will trace out the Green's function of the diffusion equation as t unfolds. As a consequence, a simple method to solve the diffusion equation, with data $q(x, 0) = g(x)$, is to sprinkle particles along the x axis with density $g(x)$, and then allow these particles to perform independent Brownian motions. This same development follows for a three-dimensional case where particles are distributed within a volume of density $g(x, y, z)$.

Comparing the Eulerian formulation of diffusion:

$$\frac{\partial q}{\partial t} = K \frac{\partial^2 q}{\partial x^2} \quad (4.4)$$

where K is the diffusivity in units $\text{m}^2 \text{s}^{-1}$ to the Green's function solution traced by the random walk in equation 4.3, one can derive a relationship between the variance given in equation 4.2 and the diffusivity, K . This allows the model to use a more physical parameter such as K . Comparing the two forms, we have:

$$c = \sqrt{\frac{2K}{\Delta t}} \quad (4.5)$$

In this manner, PUFF uses the more physically realistic parameter, K . The three-dimensional formulation used by PUFF separates K into its horizontal and vertical components, K_h and K_v as its dispersion parameter and calculates a random variable $\mathbf{Z} = (c_h, c_h, c_v)$ for each particle at each time step, using the above relationship.

4.2.3 Fallout

Ash fallout is included in the model through the last term, $\mathbf{S}_i(t) = (0, 0, s)$ in equation 4.1. The terminal speed, s , is approximated by Stoke's law and is a function of particle size through the relation:

$$s = \frac{2\rho g d_i^2}{9\eta} \quad (4.6)$$

where ρ is the density of the particle, η the dynamic viscosity coefficient, g the gravitational acceleration and d_i is the i^{th} particle's size. For simplicity, the model assumes a constant for the term $\rho g/\eta = 1.08 \times 10^9 \text{ m}^{-1} \text{ s}^{-1}$.

4.3 Model Description

PUFF was developed to provide a fast, near real-time model predicting ash cloud location and spatial dimension over some forecast period following an eruption. At its most basic level, PUFF calculates 4D trajectories, integrating the motion of a collection of ash particles over the simulation period. It goes beyond standard trajectory models, however, by including fallout and dispersion in the ash particle motion. Given a sufficient number of representative particles to provide meaningful statistical measurements, PUFF provides a reliable forecast tool to predict ash cloud migration and dispersion. Model output is a binary file representing the 3D location, size and age of each simulated ash particle, one file for each requested forecast interval beyond the eruption date. These files are suitable for processing in a number of visualization software packages, allowing site-specific tailoring of visual output.

Since PUFF is designed for emergency response, it makes simple assumptions for the default values of many of its parameters, releasing the burden to provide input that is

most likely not available during the early stages of an eruption. PUFF prompts for the most basic input requirements such as the location of the volcano and eruption time and provides, a mechanism for overriding default values if necessary. Other commonly set options include run-length, desired output interval, number of ash particles, eruption duration and plume height. There are still other, more esoteric options included in the model intended for more detailed studies of an eruption and not usually needed in an emergency-response setting.

PUFF uses SI units including Universal Time Coordinates (UTC) as its basis. Meteorological wind data typically come on standard millibar height levels and must first be converted to height levels in meters. Thus, the first task of PUFF is to pre-process the wind data. This conversion is done by interpolating onto a 4D Geopotential Height data set. If these data are missing or bad, then estimates of a standard atmosphere are made for the conversion. The conversion is done to allow particles to traverse 3D space entirely in meters and output particle heights expressed in meters instead of millibars. Other pre-processing tasks include error checking routines for patching or warning of bad data and consistency checks of input parameters.

PUFF has been compiled and executed on a variety of platforms, including Silicon Graphics R4*** series and Hewlett Packard HPUX workstations. A typical simulation for a 24 hour forecast run initializing 5000 particles on these machines requires 1 to 5 minutes of processing time. This time includes all of the separate tasks of wind data conversion, model run and the creation of graphical output.

4.3.1 Ash Particle Initialization

To begin a simulation, PUFF initializes a collection of ash particles, each of which have three basic properties: location (longitude, latitude, height), size and age. The total number of particles desired in a simulation becomes a trade-off between spatial statistics and computational time. Fewer particles require less time to simulate but provide less than ideal statistics for defining the spatial extent of the ash cloud. In practice, an ash count between 2000 and 5000 particles provides adequate statistical information while requiring a minimum of processing time to run the simulation.

PUFF initializes the position of each particle above the volcano. The height of each particle is randomly distributed from the surface (1000 mb \approx 0 m) to the top of the plume which is an option that may be set by the user. The default behavior is to initialize a column of ash particles from the surface to the maximum height of the wind data. This behavior is chosen since, in an emergency, the plume height can be difficult or impossible to measure or even estimate. Since wind speeds and direction can vary rapidly with height, an error in the initial plume height can lead to a mis-representation of the ash cloud trajectory by including (or not including) particle motion at certain levels. For warning purposes, it is safest to include and thus integrate motion over all levels. Then, when other information is available such as satellite imagery or pilot reports, the model can be re-run with the updated height estimate. PUFF provides options to initialize the vertical shape of the column to one of three possibilities: 1) linearly distributed from the surface to the plume height [Default]; 2) A Poisson distribution which preferentially loads a certain height level; 3) Exponentially distributed up to the plume height. Figure 4.2 depicts a histogram of each of these distributions initialized with a plume height of 12 kilometers.

The age of each particle is the elapsed time from when they are released at the site.

During a simulation, particles are independently released over a length of time represented by the eruption duration. The method for doing this is a random release linearly distributed over this period. The eruption duration is an option in the model which defaults to the full length of the simulation, thus simulating a continuous eruption. However, if satellite imagery or other information suggest otherwise, a “burst” eruption is simulated by setting the duration length less than the simulation length.

The ash size distribution is initialized using a gaussian shape on a logarithmic scale. The model uses two parameters which the user may modify to describe this: the base 10 logarithm of the mean size in meters and the logarithmic standard deviation, or spread, also in meters. The size of each particle determines the fall speed of that particle and PUFF only tracks particles for positive height values. Large particles typically settle to the surface within the first few time steps and the size distribution remaining aloft rapidly shifts toward smaller particles.

To demonstrate this behavior, figure 4.3 shows two simulated events with different initial size distributions. The log mean size in (a) is -3 and in (b) is -5. Both simulations used a logarithmic spread of 1.5. The histograms show the initial size distribution (darkest color tone), the distribution of particles aloft at 30 minutes (middle color tone) and at 4 hours (white). Both simulations demonstrate that within the first 30 minutes (6 steps, using a 5 minute time step) the larger particles greater than about 10^{-4} m no longer remain. The fractional difference of settled particles can be severe, the simulation in (a) loses 72% of its particles in the first 6 time steps while the simulation in (b) loses only 23% during this period. Because most applications of the model are interested in particles which can travel for several hours, the model defaults to an initial particle size centered at 10^{-5} m and a logarithmic standard deviation of 1.5 m. For many of the smaller, longer-lived particles, vertical motion can overwhelm fallout such that these particles essentially stay in the atmosphere throughout the duration of the simulation, note the difference

between 30 minutes and 4 hours in both simulations is slight.

The model currently does not consider topography when tracking ash particles since the driving wind field data generally ignore boundary-layer physics. This is not considered a limitation since the intended use of the model is for tracking upper-level airborne ash well away from boundary effects. Thus the surface is defined in the model at 0 meters and particles are only tracked until their height becomes 0 or negative.

4.4 Case Studies

This section presents some examples of PUFF simulations of three recent eruptions. These examples used archived wind data but otherwise the model runs used to generate output was the same model in operational use. The first of these is the Mount Spurr, Alaska eruption of 1992 and will be examined in more detail than the others for space and time considerations. The second example is the 1994 eruption of Klyuchevskoy Volcano, located on the Kamchatka peninsula, Russia. As a third example, the 1994 eruption of Rabaul Caldera, New Guinea is simulated to demonstrate an event in the southern hemisphere.

4.4.1 1992 Mount Spurr/Crater Peak Eruptions

On 27 June, 1992, the Crater Peak vent on the south side of Mount Spurr began a period of eruptive activity after 39 years of dormancy. This activity followed a 10 month period of elevated seismic activity. Eruptions continued on and off for the next few months, with significant ash produced in August and September eruption events. For more details of these events, see Alaska Volcano Observatory [1992] and Schneider et al. [1995].

At 2348 on August 18 UTC, a pilot reported an ash-rich plume. The main eruption followed an hour later at 0042 August 19 when strong tremor was recorded on all Spurr seismic stations. By 0058 a subplinian ash column projected ash up to 11 km altitude. Ultimately, the radar-determined plume top reached about 14 km – pilot reports were higher. Upper-level winds took the plume east-southeast directly over Anchorage, where sand-sized ash fell as thick as 3 mm. Beyond Anchorage, the axis of the plume crossed the Chugach Mountains and followed the coast toward Yakutat Bay. At Yakutat, 550 km downwind, ashfall was significant; at Juneau, 1000 km downwind, the plume was sufficiently opaque to disrupt air traffic. Ashfall forced the closing of Anchorage International Airport for 20 hours. Air-quality alerts were issued during the ashfall and on the following day, as vehicular traffic resuspended the ash.

The August eruption event was recorded on several NOAA 11 and 12 Advanced Very High Resolution Radiometer (AVHRR) satellite passes [Schneider et al., 1995]. The AVHRR instruments can record the Cook Inlet region over ten times per 24 hour period. This is the highest temporal resolution of usable satellite data available at high latitudes. The data have a spatial resolution of 1.1 km and a swath width of approximately 2400 km and the images are recorded in five wavelengths. A more detailed summary of NOAA satellite instrument characteristics is available in Kidwell, K. B., Editor [1991] and Holasek and Rose [1991]. For this event, 6 scenes over a 20 hour period following the eruption provide clear images of the ash cloud as it traversed Cook Inlet and moved east-southeast along the coast. This data set provides an excellent source for comparison and validation of PUFF model performance.

Figure 4.4 depicts two AVHRR thermal (band 4) image scenes recorded by the NOAA-12 satellite. The first scene (left) has an image date of 1992 August 19 0331 UTC (Julian day J232) and shows the plume 2:49 hours following the eruption. The ash cloud is clearly distinguishable from meteorological clouds as it traverses Cook Inlet to the east-southeast

of Mount Spurr. In these scenes, the -10°C contour is shown on the images to delineate the ash cloud. The second scene (right) at J232 1338 follows the eruption by 12:56 hours where the ash cloud has moved further down the coastline in a south-eastward direction and significantly dispersed spatially, spreading along a north-south axis.

Temperature conditions at the time of the eruption are displayed in figure 4.5 while wind vectors for three vertical levels are shown in 4.6. Both figures generated data form an interpolation of the Unidata files used in the simulation. These data are used to analyze the movement of the ash cloud and aid in comparisons to PUFF model output.

The height of the plume can be estimated by comparing plume temperatures derived from the thermal images with the atmospheric profile. Temperature comparisons between a plume and the ambient atmosphere can contain errors due to adiabatic expansion of a rising plume [Woods and Self, 1992]. Typically, the top of a plume is undercooled relative to the ambient atmosphere because the material in the ascending column rises above its neutral buoyancy height, decompresses and therefore cools. However, as material at the top of the column slumps downward, it is recompressed and warms up to the ambient temperature. This temperature anomaly therefore decays over time and is controlled primarily by the stratification of the atmosphere. Decay times are on the order of the Brunt-Vaiasala period, $1/N$, typically $10^2 - 10^3$ seconds. Thus, most material in the plume reaches the ambient temperature relatively quickly – usually within minutes – of the eruption.

The atmospheric temperature profile records temperature values of -50°C to -60°C for a range of heights between 10 and 14 km. These temperatures were observed on the first images recorded within 3 hours of the eruption. This is consistent with the initial pilot reports of an ash cloud spotted at 11 km and a later radar measurement at 14 km. Temperatures on later scenes (figure 4.4, right) record coldest plume temperatures at

around -40°C , corresponding to profile temperatures at 8 km.

Wind speed and direction can also provide clues to plume levels and dispersal. It is not uncommon for wind direction to vary with height as it does in this region during the eruption event (figure 4.6). Surface winds for this event are generally in a north to northeast direction while winds turn more to the south and increase in speed up to levels around 10 km where they are in a strong south-eastward direction. Above this level, winds turn slightly back to a more eastern direction and lessen in speed. The plume dispersal pattern seen by comparing the two image scenes (figure 4.4 suggest plume heights at all levels up to about 15 km. The second image shows a strong elongation in the ash cloud in a north-south direction where upper level winds have advected the plume to the southeast. The plume also maintains a significant amount of ash in the eastern direction suggesting a lower level component following winds below 5 to 10 km.

As stated earlier, PUFF is essentially a trajectory model with fallout and turbulent dispersion included in the motion. The turbulent diffusivity is a parameter that can be adjusted by the user. Setting this parameter to zero “turns off” the turbulent motion and the model traces out a wind trajectory for each particle. Also, setting the mean ash size to a very small value (for example, 10^{-20} m) effectively turns off the fallout motion of each particle. PUFF was used in this manner to depict trajectories at three altitudes (figure 4.7). These trajectories demonstrate what was expected from analyzing the wind field – that the vertical variations in wind direction create a north-south elongation to the ash cloud.

The PUFF simulation for this event with turbulent dispersion and fallout included is shown in figure 4.8. The time of each model run corresponds to the image scenes in figure 4.4. Each simulation initialized an ash column of 10000 particles linearly distributed in height from the surface to a maximum of 16 km. The turbulent diffusivity

was $2 \times 10^4 \text{ m}^2 \text{ s}^{-1}$ in the horizontal direction and $10 \text{ m}^2 \text{ s}^{-1}$ in the vertical direction. Ash particles are displayed as a scatter plot color-coded according to each particle's altitude. For reference, the -10°C contour from the image scenes is overlain on each figure. In the simulation, upper-level particles are seen mostly in the southern portion of the ash cloud where they have followed the southeast trajectory expected from the wind profiles. Likewise, the northern portion of the ash cloud mainly consists of lower-level ash particles following a more eastern trajectory.

As a final example of this event, figure 4.9 displays six AVHRR thermal images of the August 19 Spurr eruption with the corresponding PUFF simulation. Since PUFF is a Lagrangian tracking model, output can be tailored to any interval of time following an eruption. The input parameters are the same as those in the previous examples, however, separate ash levels are not distinguished in this figure.

4.4.2 Klyuchevskoy Volcano, October 1994

Klyuchevskoy Volcano, located on the Kamchatka peninsula about 135 km north of Petropavlovsk, Russia is one of the largest on-land active volcanos in the world and reaches an altitude of 4,739 m above mean sea level. It lies near the north end of a belt of 30 active Kamchatkan volcanos that average 3 to 5 eruptions a year. Because prevailing winds are from the west and northwest, airborne ash from these eruptions tends to move into the heavily used North Pacific (NORPAC) air routes that both cross and parallel the shoreline of the Kamchatka Peninsula (figure 4.1). These routes are used by up to 70 flights a day carrying about 10,000 passengers and large tonnages of cargo.

The 1994 eruption of Klyuchevskoy began September 8 with minor explosive activity. Reported ash clouds were below 9 km (30,000 feet) – the minimum altitude for most air

traffic in the region and thus was not of immediate concern.

This activity was followed later that month by a major eruption on September 30 (Julian day 273) at approximately 0500 UTC [Global Volcanism Network, 1994a]. This eruption disrupted air traffic across the North Pacific for the next 60 hours. An eruption column of ash and gas rose to 11 km, moving southeast into the NORPAC traffic system.

Later that day, the eruption intensified and the ash column reached 18 km by some reports. Wind speeds at the 10 to 15 km level were 40 to 50 m/sec (120 miles per hour) and generally east/southeast. The first pilot reports came at 2005 and 1010 UTC on September 30 when a thin layer of ash was reported at 163.5E, 51.5N. Many additional reports were received for the next 49 hours in NORPAC flight routes R220, R580, G583, A590 and A591.

By 1700 October 1 UTC (Julian day 274) the eruption began to subside and was no longer considered a hazard to aviation by 1700 October 2. The major explosive phase of this eruption lasted about 36 hours and was particularly intense for 10 hours between 1800 September 30 and 0400 October 1.

The NOAA 12 thermal band 4 satellite image (figure 4.10A) on Oct 1 0641 UTC shows a distinct volcanic ash plume emanating from Klyuchevskoy and extending east-southeast. Plume temperatures derived from this image range from about -40°C to 0°C on the edges. Background temperatures offshore from the volcano range from about 5°C to 20°C . Atmospheric temperature profiles record -40°C temperatures at around 8 km. Given uncertainties in measurements and field reports of plume altitudes, this is an acceptable agreement with initial estimates of 11 km. Winds in the region were generally to the east-southeast and steady (figure 4.11).

The PUFF simulation for this event is shown in figure 4.10B. The model run began at day 273 0500 UTC and ran for 25.67 hours to the image scene date at day 274 0640 UTC. The simulation initialized an ash plume 12 km high with a linear vertical distribution and continuously emitted the particles for the duration of the simulation. Ash particles in the figure are colored according to their altitude. It is evident from comparing the simulation to the thermal image that the eruption has placed ash at nearly all levels. Note particularly the dual plume in the thermal infrared image, where the main trajectory is southeast of the site while there is a smaller lobe that begins east and turns southeast about 50 to 100 km offshore. This second lobe appears to be following surface level winds where one can see from the PUFF simulation a similar trajectory for low level particles. Higher altitude trajectories follow a more direct southeast direction. Eventually, nearly all levels curve east and north far offshore at about 180E, 40N (beyond the AVHRR image region) as the winds are changing in time and space over the model run. The horizontal diffusivity was decreased in this simulation from the default value of $K_h = 2 \times 10^4 \text{ m}^2 \text{ sec}^{-1}$ to $8 \times 10^3 \text{ m}^2 \text{ sec}^{-1}$, most likely a result of strong winds (greater than 50 m s^{-1}) at the higher altitudes.

4.4.3 Rabaul Caldera, September 1994

Rabaul Caldera, located in Papua New Guinea (152.2E, 4.27S) began a series of major eruptions on Monday morning, September 19, 1994 0600 local time. This was preceded by a magnitude 5.1 earthquake at 0300 the previous morning followed for the next 27 hours by unusual seismic activity [Global Volcanism Network, 1994b].

The eruptions began with Tevurvur (one of three principal cones in the Rabaul Caldera Complex), followed later by an eruption of the Vulcan Volcano, sending ash according to one report 18 km high. Within 24 hours, ash depths in nearby cities were reported one half

to 2 meters thick. Several thousand residents of Rabaul were evacuated within these first few hours. Eruptions continued for the next few days, subsiding slightly by Wednesday, September 21 and renewing in strength again by Thursday. Both Japan Airlines and Korean Air were forced to reroute their Asian-Australian flights to avoid the plume.

Satellite images showed the main plume 20 hours following the initial eruption dispersing in a broad fan shape to the west and southwest. The NOAA-12 thermal band 4 image for September 19 0859 (day 262) UTC is shown in figure figure 4.12A. The PUFF simulation of this event is shown in figure 4.12B, driven by measured wind values from archived Unidata sources.

Upper level winds during the eruption were generally steady and trended west-southwest, circulating around a divergent region centered at approximately 155E, 10S (figure 4.13). Surface winds were light (about 5 m/sec) and variable. This event was fortunate enough to have the Space Shuttle (STS-64) in orbit which was able to take excellent photographs of the eruption. These photos (not shown) suggest the plume was rapidly emplaced at higher altitudes and flattened in a distinct layer, most likely at the tropopause around 16 km. This would explain the simulation results depicting a low altitude lobe moving to the north-northeast at levels below 6 km with no counterpart seen on the AVHRR image. Also, this was a large eruption and likely placed ash well above the Unidata limit of 100 millibars (approximately 16 km). Such particles might be detected on satellite images but the model would have no way to simulate these without using another data set. Mid to upper level particles (6 to 16 km) correlate well with the plume seen on the image. For this simulation, the horizontal diffusivity was increased to $K = 8 \times 10^4 \text{m}^2 \text{sec}^{-1}$ to adequately depict the broad fan shape.

Observations of various images collected during this eruption suggest a two-lobed plume which could be interpreted as a bifurcation [Ernst et al., 1994]. This occurs when

a bent-over plume with its own momentum is distorted by a cross current, developing a vortex structure which bifurcates the plume into two divergent lobes. This effect can be enhanced near a density interface such as the tropopause. Since PUFF does not include any source physics such as buoyant effects or initial momentum, in the model's current form, this effect can not be simulated. However, even in laboratory experiments, the first order motion of a bifurcated plume is advection which is why the simulation results are in good agreement with the imagery.

4.5 Conclusions

This paper presented the technical background of a Lagrangian ash tracking and prediction model. The model was designed for operational use during an eruption to provide near real-time forecasts of ash movement. Several examples of recent eruptions were used for comparison to simulation results and to validate the model. These examples show good agreement with plumes observed on satellite images. Other sources of information such as vertical temperature and wind profiles are useful for interpreting results. The model does not include any source physics such as thermal buoyancy or initial momentum and therefore could not resolve such behavior. However, in most cases plumes cool to the ambient temperature and show wind driven motion very soon after initial emplacement. In such conditions, this model provides a reliable forecast tool during an eruption.

Acknowledgments

The authors would like to thank Dave Schneider and Kevin Engle for providing AVHRR image data and Kevin Engle for his assistance in data processing. This research was

funded in part by a Cooperative Program for Operational Meteorology, Education and Training (COMET) Partners Project. Additional support was provided by the Alaska Volcano Observatory, USGS and the Geophysical Institute, University of Alaska Fairbanks. Figures for this manuscript were produced using the public domain software, Generic Mapping Tools (GMT) [Wessel and Smith, 1995].

References

- Alaska Volcano Observatory (1992). Mt. Spurr's 1992 eruptions. *EOS Trans. Amer. Geophys. U.* 74(19), 217–222.
- Casadevall, T. J. (1994). The 1989-1990 eruption of Redoubt Volcano, Alaska: impacts on aircraft operations. *J. Volc. and Geotherm. Res.* 62, 301–316.
- Dean, K. G., S. Bowling, G. Shaw, and H. Tanaka (1994a). Satellite analyses of movement and characteristics of the Redoubt Volcano plume. *J. Volc. and Geotherm. Res.* 62, 339–352.
- Dean, K. G., L. Whiting, and H. Jiao (1994b). An aircraft encounter with a Redoubt ash cloud. In T. J. Casadevall (Ed.), *Proceedings of the First International Symposium on Volcanic Ash and Aviation Safety*, U.S. Geological Survey Bulletin, Number 2047, pp. 333–339.
- Ernst, G. J., J. P. Davis, and R. S. Sparks (1994). Bifurcation of volcanic plumes in a crosswind. *Bull. Volcanol.* 56, 159–169.
- Etlings, D., J. Preuss, and M. Wamser (1986). Application of a random walk model to turbulent diffusion in complex terrain. *Atmospheric Environment* 20, 741–747.
- Global Volcanism Network (1994a). Kliuchevskoi. *Bulletin of the Global Volc. Network* 19(9), 2.

- Global Volcanism Network (1994b). Rabaul. *Bulletin of the Global Volc. Network* 19(9), 4-7.
- Heffter, J. L. and B. J. Stunder (1993). Volcanic ash forecast and dispersion (vaftad) model. *Weather and Forecasting* 8, 533-541.
- Holasek, R. E. and W. I. Rose (1991). Anatomy of 1986 Augustine Volcano eruptions as recorded by multispectral image processing of digital AVHRR weather satellite data. *Bull. Volcanol.* 53, 420-435.
- Kao, C.-Y. and T. Yamada (1988). Use of CAPTEX data for evaluations of a long-range transport numerical model with a four-dimensional data assimilation technique. *Mon. Weath. Rev.* 116, 293-306.
- Kidwell, K. B., Editor (1991). *NOAA Polar Orbiter Data Users Guide (TIROS-N, NOAA-6, NOAA-7, NOAA-8, NOAA-9, NOAA-10, NOAA-11, AND NOAA-12)*. Princeton Executive Square, Rm. 100, Washington D.C. 20233: National Oceanic and Atmospheric Administration - National Environmental Satellite Data and Information Service - National Data Center, Satellite Data Services Division.
- Peterson, R. A. and J. D. Stackpole (1989). Overview of the NMC production suite. *Wea. Forecasting* 4, 313-322.
- Physick, W. L. and D. J. Abbs (1991). Modeling of summertime flow and dispersion in the coastal terrain of south-eastern Australia. *Mon. Weath. Rev.* 119, 1014-1030.
- Rolph, G. D. and R. R. Draxler (1990). Sensitivity of three-dimensional trajectories to the spatial and temporal densities of the wind field. *J. Appl. Meteor.* 29, 1043-1054.
- Schneider, D. J., W. I. Rose, and L. Kelly (1995). Tracking of 1992 eruption clouds from Crater Peak Vent of Mt. Spurr Volcano, Alaska, using AVHRR data. In T. Keith (Ed.), *The 1992 Eruptions of Crater Peak Vent, Mount Spurr Volcano, Alaska: U.S. Geologic Survey Bulletin*, Number 2139, pp. 27-36.
- Tanaka, H. L. (1991, July 8-12). Development of a prediction scheme for the volcanic ash fall from Redoubt Volcano. In *First International Symposium on Volcanic Ash*

- and Aviation Safety, Seattle Washington.* U.S. Geological Survey Circular 1065, pp 58.
- Tuck, B. H. and L. Huskey (1992). The economic consequences of the 1989-90 Mt. Redoubt eruptions. Technical report, Institute of Social and Economic Research, University of Alaska Anchorage.
- Wessel, P. and W. H. F. Smith (1995). New version of the Generic Mapping Tools released. *EOS Trans. Amer. Geophys. U.* 76, 329.
- Woods, A. W. and S. Self (1992). Thermal disequilibrium at the top of volcanic clouds and its effect on estimates of the column heights. *Nature* 355, 628-630.

Figures

4.1	North Pacific area map	67
4.2	Three possible vertical plume distributions	68
4.3	Two ash size distributions	69
4.4	Mount Spurr AVHRR thermal infrared images	70
4.5	Mount Spurr temperature profile	71
4.6	Mount Spurr wind vectors	72
4.7	Mount Spurr ash trajectories	73
4.8	Mount Spurr PUFF simulation	74
4.9	Mount Spurr PUFF simulation mosaic	75
4.10	Klyuchevskoy Volcano AVHRR thermal infrared image and PUFF simulation ..	76
4.11	Klyuchevskoy Volcano wind vectors	77
4.12	Rabaul Caldera AVHRR thermal infrared image and PUFF simulation	78
4.13	Rabaul Caldera wind vectors	79

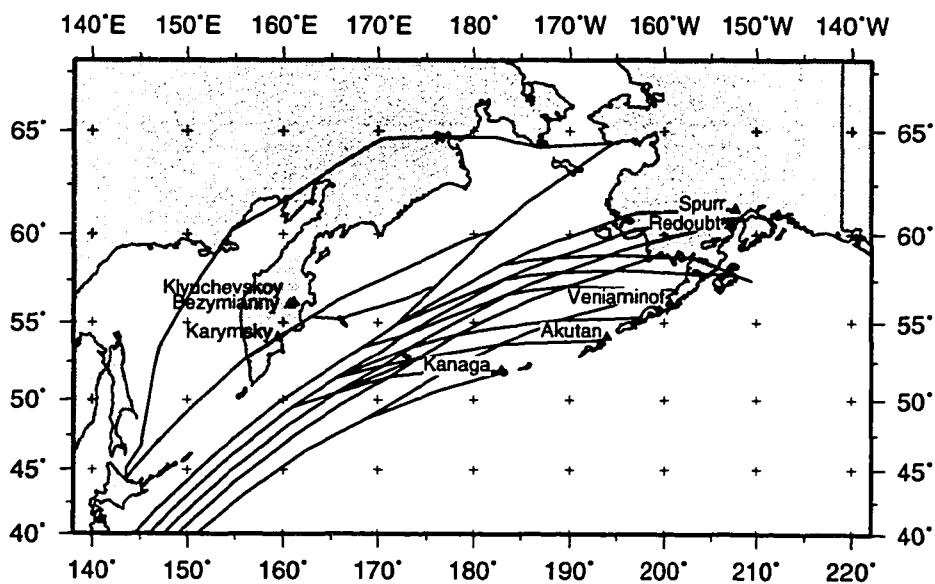


Figure 4.1 The North Pacific Ocean region depicting NORPAC air routes and some of the volcanos displaying significant activity within the last few years.

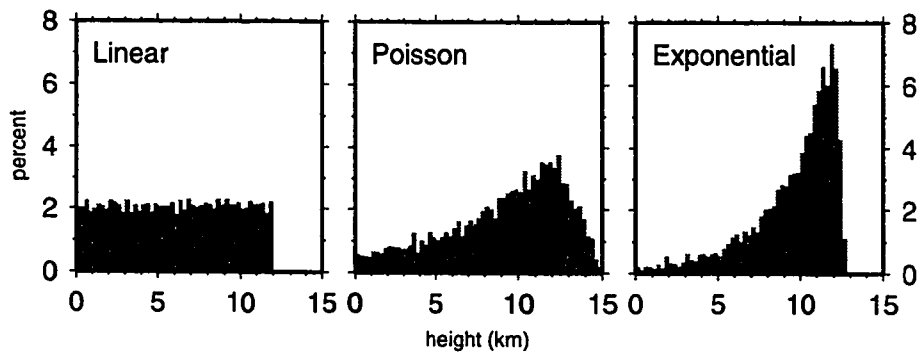


Figure 4.2 Three possible vertical ash distributions in the PUFF model. In this example, all three were initialized with a plume height of 12 km.

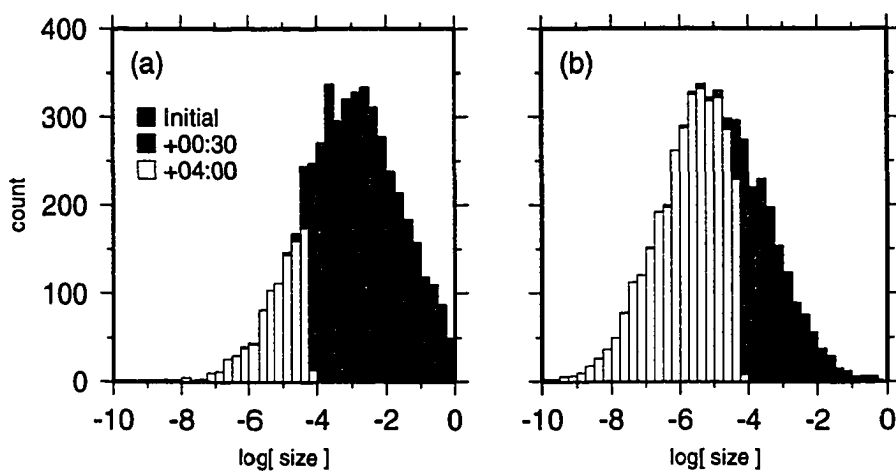


Figure 4.3 Two ash size distributions with different mean value. The darkest tone represents the initial size distribution and displays the size distribution of particles remaining aloft after 30 minutes (middle tone) and 4 hours (lightest tone). This demonstrates that particles greater than about 10^{-4} m typically fall out within the first few time steps and remaining particles exist throughout most of the model run.

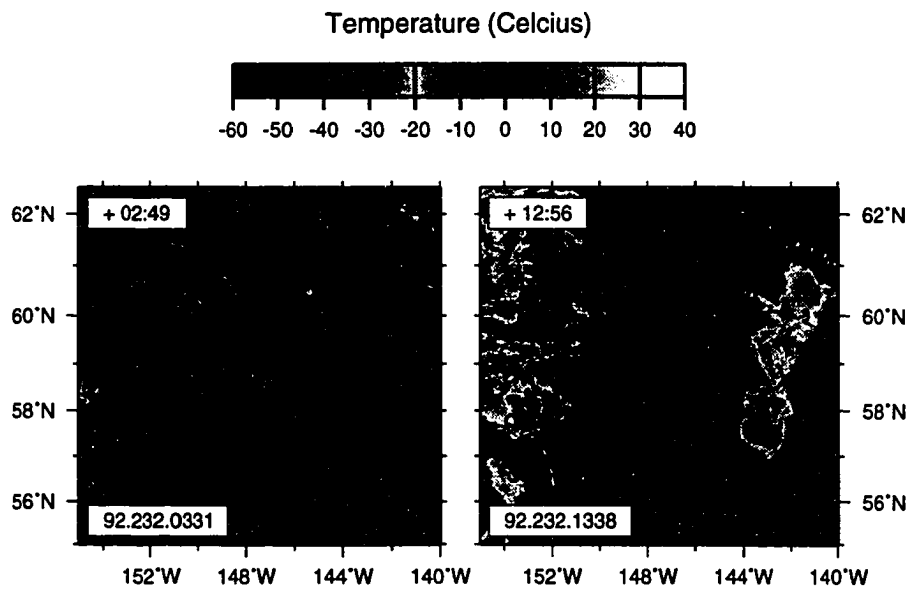


Figure 4.4 AVHRR thermal infrared (band 4) satellite images of the 1992 September eruption of Mount Spurr/Crater Peak. The left image is 2:49 hours following the eruption while the right follows by 12:56 hours. Absolute image times are given in the lower left corner.

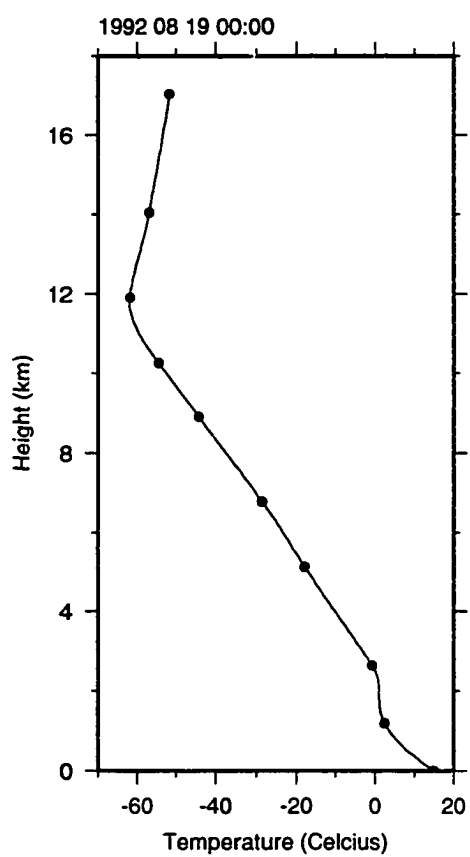


Figure 4.5 The vertical temperature profile at Mount Spurr (207.75E, 61.3N - 08/19/00:00 UTC) interpolated from measured Unidata values.

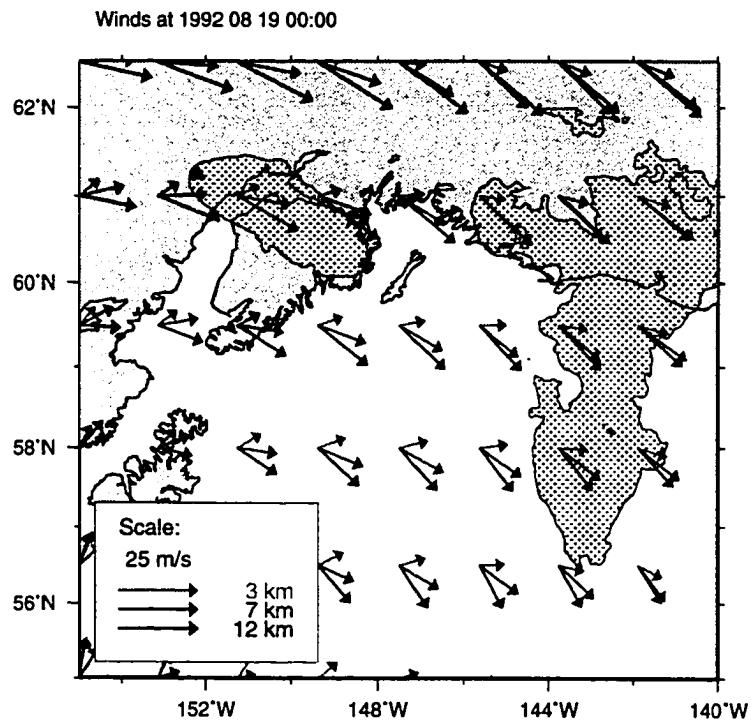


Figure 4.6 Wind vectors at three vertical levels for the Mount Spurr region. The hatched regions correspond to the -10°C contours in figure 4.4.

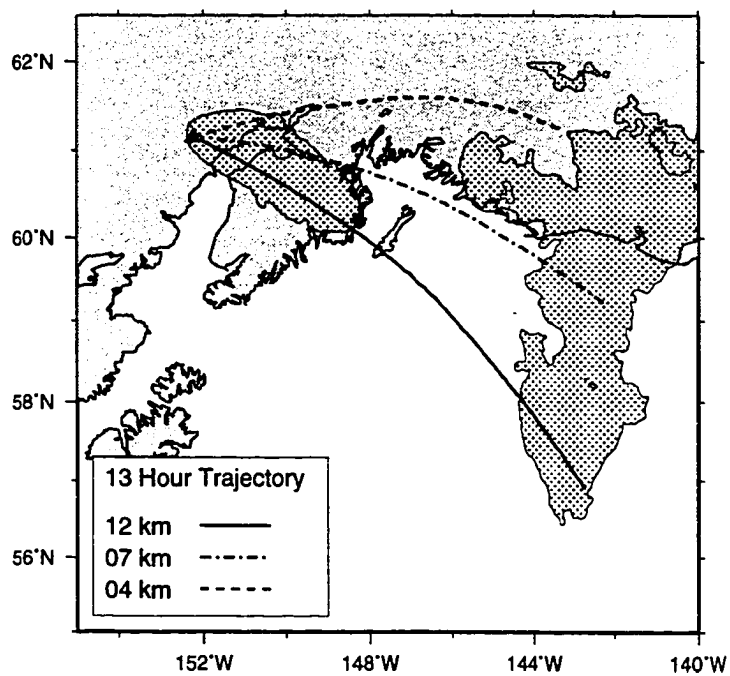


Figure 4.7 Single particle PUFF derived ash trajectories at three levels for a 13 hour simulation. The hatched regions correspond to the -10°C contours in figure 4.4.

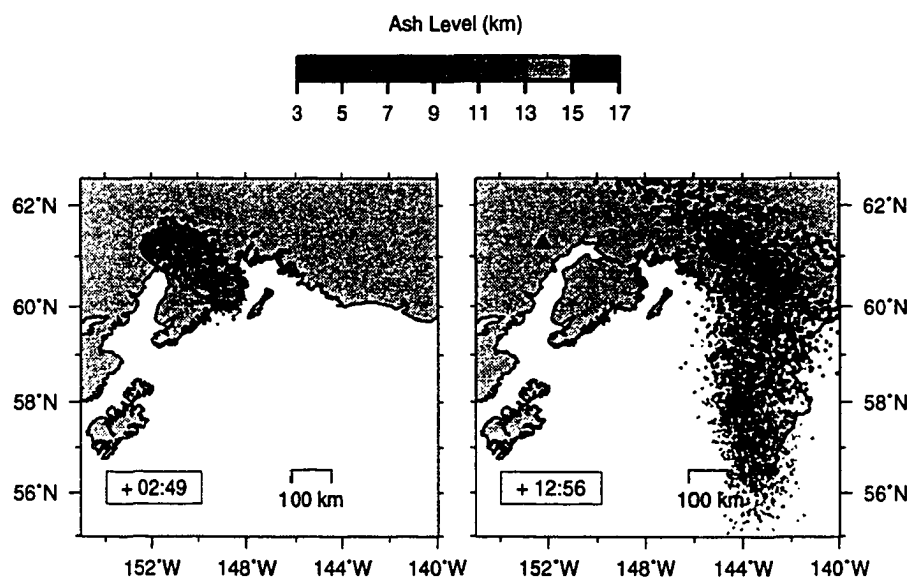


Figure 4.8 PUFF simulation of the Mount Spurr eruption. The simulation times correspond to the image scene dates shown in figure 4.4. The ash particle altitude is color-coded. Overlain are the -10°C contours derived from figure 4.4 for comparison.

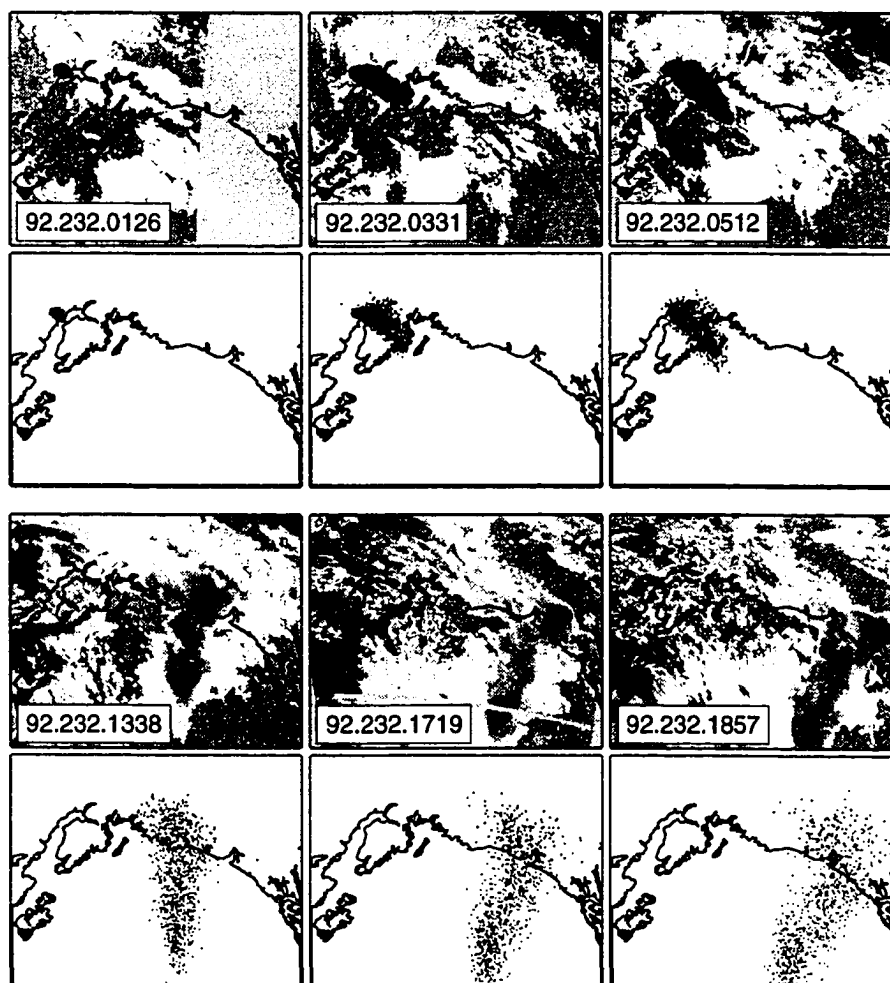


Figure 4.9 A mosaic of six AVHRR thermal infrared satellite images of the 1992 19 August Mount Spurr eruption with the corresponding PUFF simulation at each time shown below for comparison.

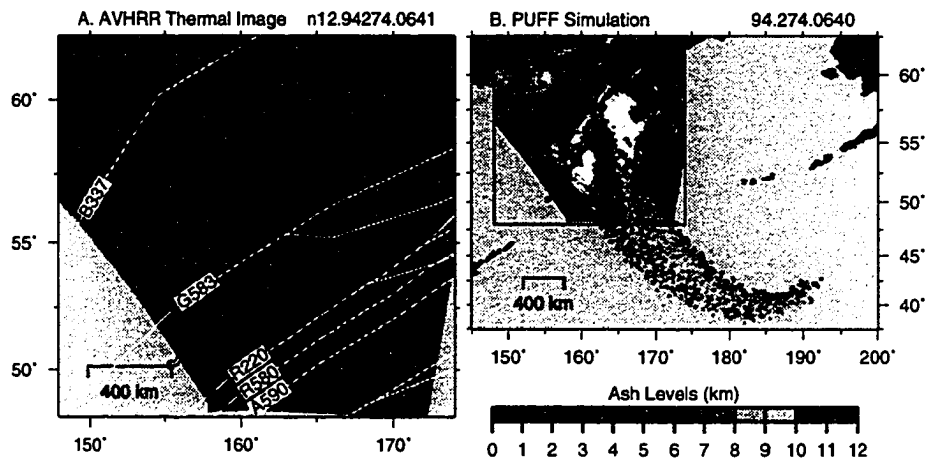


Figure 4.10 Klyuchevskoy Volcano AVHRR thermal infrared satellite image (A) and the corresponding PUFF simulation (B). Disrupted air traffic routes are overlain on the image scene (A).

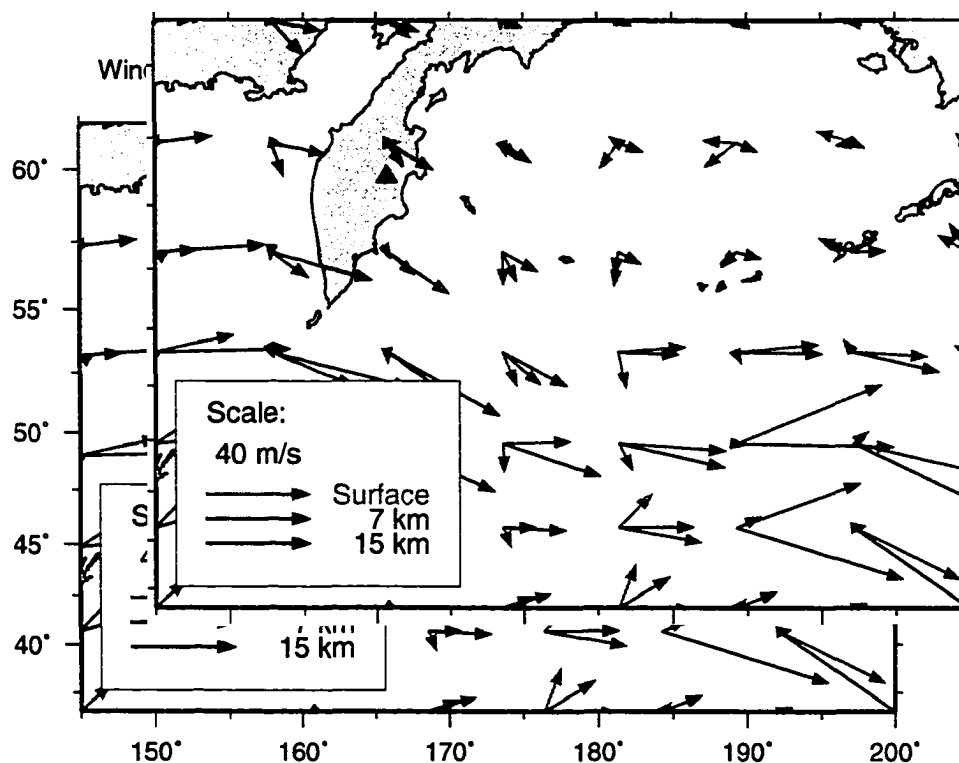


Figure 4.11 Wind vectors at three vertical levels for the Klyuchevskoy Volcano region.

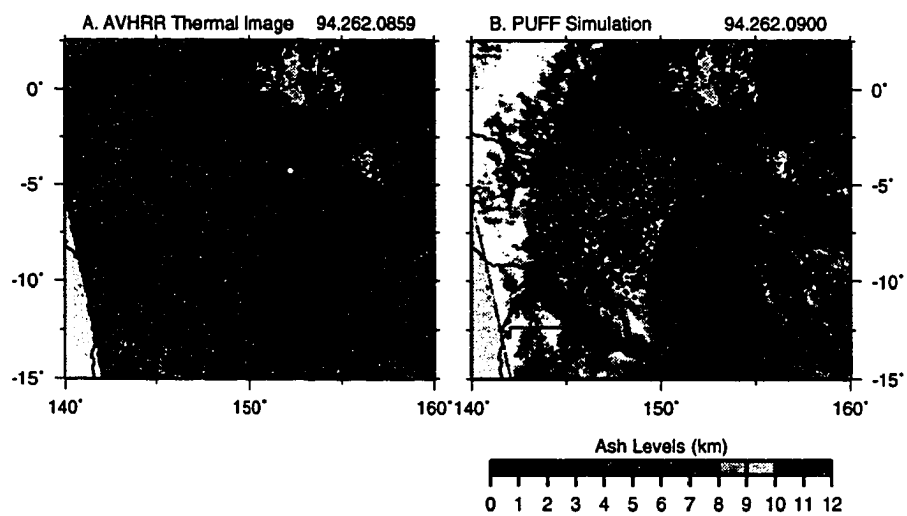


Figure 4.12 Rabaul Caldera AVHRR thermal infrared satellite image (A) and the corresponding PUFF simulation (B).

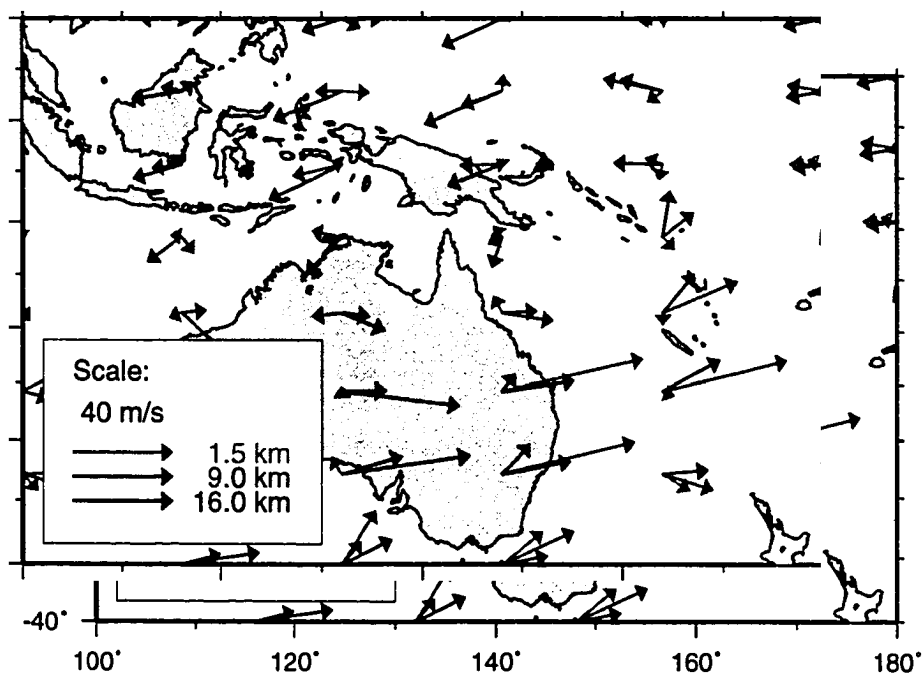


Figure 4.13 Wind vectors at three vertical levels for the Rabaul Caldera region.

Chapter 5

Discussion

This chapter follows-up on the presentation of the two case studies to discuss aspects of each study in the context of merging remotely sensed data with numerical models. Since the models were presented in detail, figures, equations and some text here may refer back to those chapters to avoid repetition.

5.1 Nearshore Ice Removal, Mackenzie River Delta

The main objective of this model (chapter 3) was to parameterize the heat supplied by the river discharge to the base of the ice cover. The model considered only those changes to the ice cover due to thermal forcing typical of an arctic spring (late May to mid-July). It also focused on the influence of discharge to the shorefast ice only, ignoring the pack ice. Heat fluxes on the upper and lower surfaces of the ice cover were parameterized separately to distinguish between atmospheric heat exchange and the sensible heat supplied by the river.

The data set used in the model was a series of AVHRR images depicting the 1986 spring breakup of the Mackenzie River Delta. The AVHRR data were exploited for their large regional coverage and high temporal resolution. The 1986 season was chosen for its relatively cloud-free conditions, supplying excellent temporal coverage through the breakup season. Typical AVHRR images used in this study (not in the original paper) are shown in figures 5.1, 5.2 and 5.3. A series of generalized schematic diagrams derived from the visible band satellite images depicting the breakup season in the Mackenzie River Delta was shown in figure 3.2. The schematics highlight spatial patterns as they change and progress through the breakup season.

5.1.1 Satellite Observations and Model Development

Of particular importance in the model was the region of water immediately adjacent to the coast. The question is asked whether this is flooded ice or open water since the mechanism of ice melt, that is solar absorption versus sensible heat, is dependent on the answer. Also, if it is flooded ice, does this account for all or only part of the river discharge? The spatial coverage of the imagery easily provides a quantitative measure of the area of open water and a time sequence of this is obtained using the set of images. There is seen on the imagery (or schematic, figure 3.2) a recession of water that coincides with the peak of discharge at approximately 4 June. This recession of water seen on the ice cover is presumably due to initial flooding and subsequent draining after the peak discharge. Therefore, at least some of the water is flooded ice. The estimation of the volume of water seen on top of the ice can be derived using the area measured from imagery and an estimate of the depth of overflows. Using a generous estimate of 1 meter depth for the overflows and comparing this amount of water to the actual 1986 discharge measurements, it was found that the observed water can only account for about 10% of the total river input. Therefore, most of the river discharge must still be accounted for, which leads to the conclusion that it is flowing underneath the ice cover which cannot be

directly observed on the images.

This quantity of water flowing underneath the ice cover was instrumental in designing the model. Since as it was argued in chapter 3 that the Mackenzie discharge is sufficient to keep the basin filled with riverine water over a time scale much shorter than the breakup season, it was decided that vertical melting was a more significant component of ice removal than lateral melting. This behavior can also be observed in a qualitative fashion on the imagery. The lateral melt away from the coast proceeds at a slow rate until, at some point, the ice cover just seemingly disappears. The model was developed to consider only the vertical melt of the ice cover as a result.

There is another aspect in designing a simple vertical-melt model. Sophisticated three-dimensional numerical schemes could be developed for the fluid dynamics of the basin but at best (at least in this case) there can only be ancillary data for input to such a model or for verification of the model, since imagery cannot provide information beneath the ice cover. Instead, in the simpler vertical-melt formulation, the main input parameter would be the temperature of the river water, which can be directly measured on the thermal image data at the point where the river enters the basin.

5.1.2 Satellite Observations and Model Parameters

In parameterizing the river sensible heat input, four terms in equation 3.2 - f_{int} , u , ΔT and C , were not directly known. These terms were estimated using geometrical arguments, direct satellite measurements and timing constraints on the breakup of the shelf ice. The first two of these terms, the interaction ratio f_{int} and the relative speed u , were estimated using geometrical arguments and discharge measurements. The discussion of these two parameters will not be repeated here, see chapter 3 for the complete discussion.

The thermal forcing, ΔT , requires the temperature of the river water discharge, T_{plume} ,

in contact with the base of the ice cover. This is spectral data extracted directly from the calibrated thermal band of the 1986 sequence of images. The river temperature is taken at a point where the river enters the basin, seen as open water areas immediately adjacent to the coast (Figure 3.2, labeled 'Overflow/Open Water' on the 4 June schematic). Using the temporal variability of the images, a time sequence of T_{plume} is derived. The temperature is seen to progress from 0°C to 1°C near the peak of discharge (1 June) to 10°C thirty days later when the Mackenzie River delta region was largely free of ice. Thus, the thermal forcing parameter is extracted directly from the imagery and given a time dependence in the model.

The last parameter to discuss is the heat transfer coefficient, C_s . Typically, given a known melt rate, dh/dt , one arrives at this parameter by measuring the bulk flow parameters u and ΔT , and reversing equation 3.2 to solve for C_s . This method eliminates the need to estimate the heat flux from turbulent temperature and velocity fluctuations or from the mean temperature and velocity profiles beneath the ice cover, which would of course require extensive field measurements.

Estimating this parameter represents a case of 'model tuning'. With all of the other model variables accounted for, the model could be run with different values of C_s , comparing results to observations. Theoretical and experimentally derived values may provide a 'first guess' for the input value in the initial model run. The model predicts when the ice cover melts completely (thickness $h = 0$). Using the temporal sequence of the images, the predicted date of removal can be compared to the actual date as seen on the imagery, giving a 'best estimate' or range of values for the unknown parameter.

5.2 A Dynamic Model of Volcanic Ash Dispersion

In the second case study, chapter 4, a dynamic pollutant tracer model was presented. This model was developed for the simulation of young ash clouds of volcanic origin. The model is intended for use as an emergency response tool in the event of an eruption near populated areas or aircraft routes.

The PUFF model introduces another aspect of merging remotely sensed data with numerical simulations – validation of model accuracy. This procedure requires the developer to either visually compare the simulation to the imagery to verify that they are in reasonable agreement or to directly compare some measurable quantity. Also, the sensitivity of model variables can be evaluated using this technique, by changing their values during successive simulations and comparing the resulting effects to some ‘baseline’.

5.2.1 Satellite Observations and Diffusivity

One key element of the model is the diffusivity of the ash cloud. This was parameterized by imposing a random walk on a collection of discrete ash particles such that a sufficient number of them will represent the concentration of an ash cloud as it disperses. The diffusivity, K , (from equation 4.3) gives a measure of the expected spreading of the ash cloud through turbulent mixing as it is advected downwind. This is a parameter which is not directly known but that affects some physically measurable quantity in the satellite imagery, that is, the width of the eruption cloud as a function of either time or distance from its source. To ‘tune’ the model, successive runs can be performed with varying values of K until the cloud width agrees with image observations.

To tune a model for a specific parameter successfully, it is desirable to use as many images as possible. This presents a difficulty since volcanic eruptions are not frequent

occurrences. Also, satellite observations can be limited by weather. It should also be noted that turbulent diffusion is highly dependent on atmospheric conditions such as stratification which can vary widely from day to day. Keeping this in mind, it should be sufficient to make an approximation with only a few images of eruption clouds and using this as a starting point for real-time simulations of future eruptions as well as further research.

The Mount Spurr eruption was fortunate to have excellent satellite coverage, allowing excellent parameter testing and model validation. Figure 4.9 depicts six AVHRR satellite images with the model results for comparison. To demonstrate the sensitivity of changing the value of K , the theoretical formulation for the spreading of the ash cloud expects a power-law dependence on K . As an example, given that the Mt. Spurr eruption lasted about four hours, with an average horizontal wind speed of 10 m s^{-1} , an order of magnitude change in K from 1×10^3 to $1 \times 10^4 \text{ m}^2 \text{ s}^{-1}$ would result in a 30 km difference in the observed width of the ash cloud four hours after erupting. A factor of two difference in K results in a cloud width difference on the order of 10 km, which is still within the 1.1 km resolution of AVHRR imagery. However, measurements of the cloud width from the images can still be a subjective process since ‘hand-choosing’ the coordinates defining the width of the ash cloud may be necessary as plume boundaries may not be clearly defined.

Figure 5.4 shows a detail of the first three image scenes from figure 4.9. The PUFF simulation of the event is shown alongside the image scenes in each figure for comparison. It is found that a value of $K_h = 4 \times 10^4 \text{ m}^2 \text{ s}^{-1}$ results in the best agreement with image data. The vertical diffusivity is much harder to measure since it is on the same order of magnitude as vertical advection. It is, however, expected to be orders of magnitude lower than the horizontal value given the nature of atmospheric turbulence. For this reason, a value of $K_v = 10 \text{ m}^2 \text{ s}^{-1}$ is maintained throughout this analysis.

5.2.2 Satellite Observations and Plume Heights

Another use in merging satellite images with the ash cloud tracking model is the estimation of the plume height. The predicted movement of the plume can be critically dependent on this input parameter since it is not uncommon for the winds to be in completely different directions at altitudes separated by as little as 1-2 km.

The heights of volcanic plumes can be estimated from temperatures extracted from calibrated thermal infrared images. The plume, which is hot when first emitted, will rise due to buoyancy but can also be propelled mechanically upward by the force of the eruption. These two factors often propel it to altitudes higher than many meteorological clouds. The eruption cloud rapidly cools to the ambient temperature due to entrainment of air and adiabatic expansion. By comparing the temperature of the upper surface of the eruption cloud derived from thermal (band 4) images to the temperature profile of the atmosphere from balloon-launch measurements (available in Unidata), an estimated height for the eruption cloud can be determined.

Alternatively, the heights of the volcanic plumes can be estimated from wind profiles in a trial-and-error fashion. The wind direction and speed usually varies with altitude and disperses the ash cloud accordingly. By comparing the trajectory to those on the simulation that correspond in time to the image, an estimate of the height can be achieved (see figure 4.7 for example). Note, however, that this will not work if there are no significant altitudinal variations in which case the height can generally only be bracketed between certain levels. This method also relies on the accuracy of the meteorological forecasts.

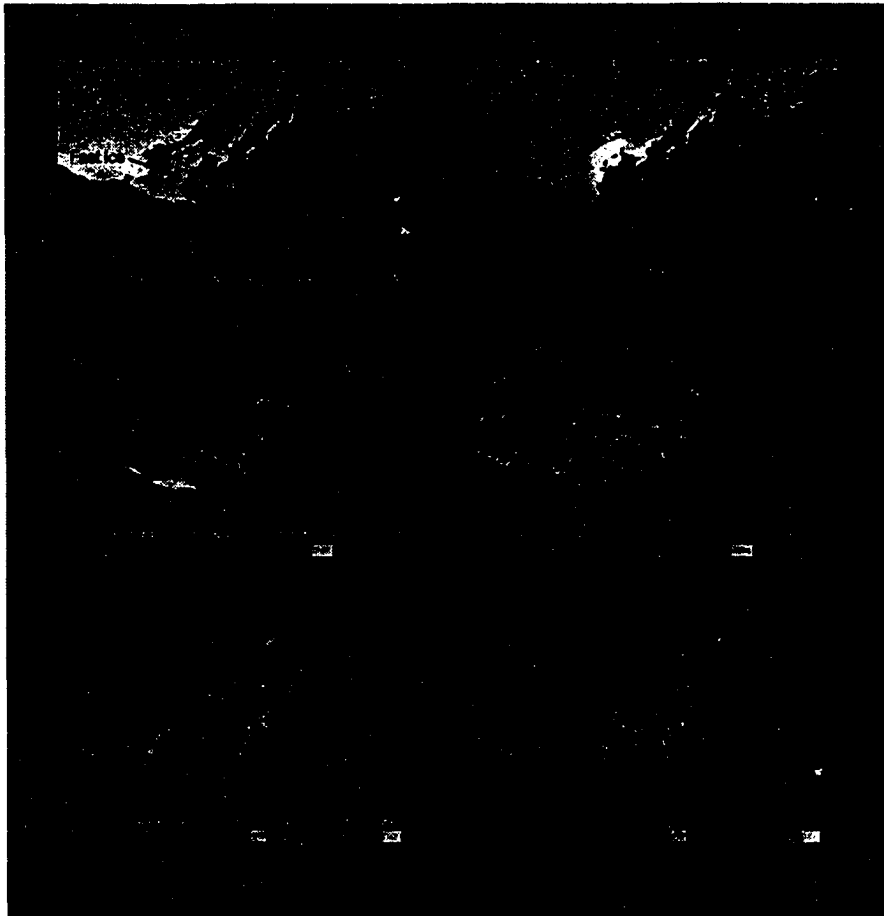


Figure 5.1 AVHRR satellite images recorded on 17 April 1986 (left column) and 25 May 1986 (right column) of the Mackenzie River delta region. The top images are color composites using the visible (B1), near-infrared (B2), and thermal infrared (B4) bands of data. The center images are the visible band data that have been color coded to show albedo. The bottom images are the thermal band data that have been color coded to show temperatures.



Figure 5.2 AVHRR satellite images recorded on 4 June 1986 (left column) and 14 June 1986 (right column) of the Mackenzie River delta region. The top images are color composites using the visible (B1), near-infrared (B2), and thermal infrared (B4) bands of data. The center images are the visible band data that have been color coded to show albedo. The bottom images are the thermal band data that have been color coded to show temperatures.



Figure 5.3 AVHRR satellite images recorded on 5 July 1986 (left column) and 16 August 1986 (right column) of the Mackenzie River delta region. The top images are color composites using the visible (B1), near-infrared (B2), and thermal infrared (B4) bands of data. The center images are the visible band data that have been color coded to show albedo. The bottom images are the thermal band data that have been color coded to show temperatures.

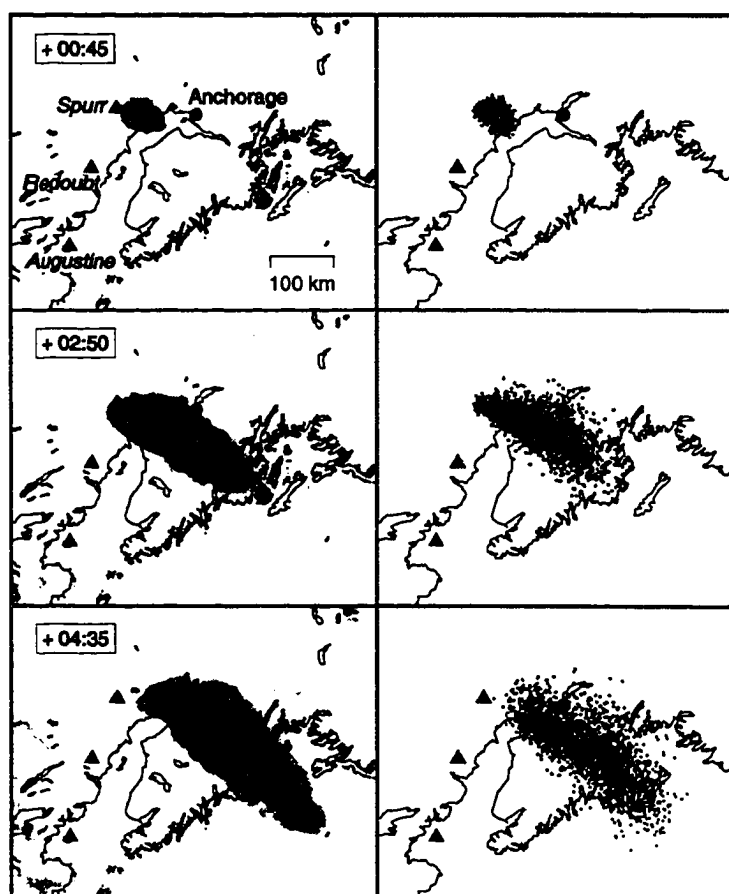


Figure 5.4 AVHRR imagery of the August 1992 Mount Spurr eruption (left column). These images depict the plume as it traverses and spreads across Cook Inlet up to three and a half hours after the eruption. The simulation of each image date is shown in the right column with ash displayed between 9 and 16 km.

Chapter 6

Summary

This thesis presented two major studies in manuscript form (chapters 3 and 4) representing the significant accomplishments of my doctoral program at the Geophysical Institute, University of Alaska Fairbanks. The concept of merging remotely sensed data with geophysical models came from recognizing that there was a certain methodology consistent to each separate development.

These two case studies illustrate how models can be designed to rely on parameters that can be provided by satellite imagery by carefully examining the information that the images make available. This contrasts with the more traditional approach of designing a 'complete' physical model and then seeking the required parameter values.

Spatial, temporal and spectral information derived from satellite imagery also provide observations used as input to model parameters or as constraints to validate model results of physical processes. This information can be a simple definition of the position and shape of specific features or the identification of time limits that must be imposed on a modeled process. Satellite imagery can also provide quantitative spectral data for direct input to model variables.

In the example of a river-ice interaction model (chapter 3), the imagery identified the timing of ice removal, spatial patterns of ice removal, and the thermal input of the discharge. The collected imagery depicting the breakup season influenced decisions made as to the specific development of the model by highlighting the known and less-known parameters. These parameters could be available as input to the model or as parameters that can be compared with model predictions. In either case, the model was initially developed to take advantage of what is well-grounded in the quantitative and qualitative contributions of the image sequence.

In the example of an eruption cloud model (chapter 4), the imagery defined the geographical limits of the cloud as a function of time. This includes defining the position of the ash cloud as well as its spreading rate. Images from numerous eruptions were examined to determine the best estimate for the diffusivity parameter, K , used in the model. A better formulation for K could be made using theoretical derivations and correlations to such parameters as wind speed and shear. Image data would still provide the best method for validating a more sophisticated formulation. The imagery combined with meteorological data can also provide an initial estimate of the height of the eruption cloud, another important input parameter.

In both case studies, the imagery made an important contribution to validating model results by providing a reference data set to 'tune' or 'calibrate' model parameters. This is done by fixing as many variables as possible to isolate the effects of model behavior to a limited number of variables. The model can then be run, successively varying input values for unknown parameters, and comparing results with the image data set. This can be performed until satisfactory agreement between model output and the image data set is achieved. Until model output is calibrated in such a manner, predictions derived from the model can at best be subjective. And, once calibrated, model sensitivity to certain parameters can be tested by again successively varying input to determine its effect on the output as measured against the calibrated baseline.

Appendix A

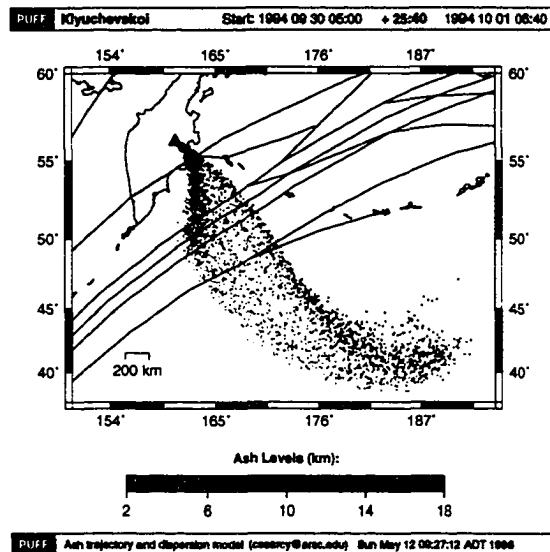
The PUFF System Manual

The PUFF model discussed in chapter 4 was part of a development of operational software beyond the scope of the research involved. This software has been used successfully at the Geophysical Institute during recent eruptions. Also, the National Weather Service funded part of the development through a COMET project and the forecast office in Anchorage, AK has implemented the software as part of their Aviation service. Since the software development represented a significant amount of work not detailed in any of the research discussed in this thesis, I have included the manual here as representative of this body of work.

PUFF

Software for the simulation and tracking
of volcanic ash clouds

Unix version 2.0



Craig Searcy
May 1996

Contents

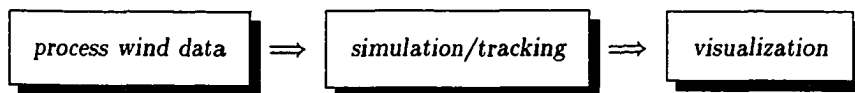
THE PUFF SYSTEM	96
Introduction	96
Requirements	96
Data Formats	97
Running PUFF	97
THE PUFF MAN PAGES	99
ashbin	100
ashdump	101
ashview	102
puff	105
fgconv	108
fgdump	112
traject	114
uni2puff	117
uniconv	119
unipack	120
uniprof	121

THE PUFF SYSTEM

INTRODUCTION

The **puffsystem** comprise a set of routines for tracking volcanic ash clouds following an eruption. These routines are intended for use as an emergency response tool in the event of an eruption near populated areas or aircraft routes. The model requires near-real-time wind forecast data (currently *Unidata*) to predict the ash cloud migration.

Simulating an eruption event and tracking the ash cloud with the **puffsystem** is a three-step process:



Each step of the process has well-defined input/output. The first step converts input wind field data for use in the second step which simulates the movement of the ash cloud and saves the state of the cloud to a separate file at requested intervals. The third step processes the saved binary ash files for visualization. Currently, the routines **uni2puff**, **puff** and **ashview** implement these steps, respectively.

The **puffsystem** is organized in this modular fashion to allow for changes in input data format, system software, visualization requirements, etc with a minimum amount of effort.

This manual describes the operation of the **puffsystem** set of routines. For technical detail of the model and numerous examples, see the document *PUFF: a high resolution volcanic ash tracking model*, Searcy *et al*, submitted to *Journal of Volcanology and Geothermal Research*, May 1996.

REQUIREMENTS

For installation, see the *README* file in the puff directory.

At a minimum, the **puffsystem** requires a C++ compiler to install. Compilation requires the **netcdf** libraries (and possibly the **HDF** libraries) for input/output of wind data and ash files.

For operations, the **puffsystem** requires real-time access to a four-dimensional wind data set such as *Unidata*.

Additionally, the visualization routine **ashview** currently requires the public domain **GMT-SYSTEM** software for the mapping of ash data. **ashview** may also require the public domain

Version: 2.0

Last change: May 1996

Ghostscript and **pbmplus** software for the conversion of postscript to a GIF image format.

DATA FORMATS

The routine **puff** requires as input gridded, four-dimensional **netcdf** data for the longitudinal (U) and latitudinal (V) wind speeds. These data must be on a (*ftime,height,latitude,longitude*) grid with *longitude* varying fastest in the binary data portion. Grid sizes are flexible, but units are expected to be (*hours, meters, degrees.north, degrees.east*). The file should contain a 16-character string variable named *reftime* in the format "YYYY MM DD HH:MM". This is the reference time of the data set in Universal Time Coordinates (UTC). The *ftime* dimension is expected to be in *hours* past the *reftime* variable. Additionally, the file may contain values for a *fill_value* variable and a *valid_range* array.

The default data set for the **puffsystem** is *Unidata*. This is a global, four-dimensional NMC data product in **netcdf** format. *Unidata* requires some pre-processing before running **puff**. The routine **uni2puff** accomplishes this task. *Unidata* is on the required (*ftime,height,latitude,longitude*) grid, however the vertical *height* level units are *millibars* (or *hectopascals*) instead of the required *meters*. **uni2puff** converts this dimension by interpolation using the *Unidata* geopotential height (H) data set. If this data is not available, **uni2puff** allows for a simple approximation. Additional tasks of **uni2puff** are sub-sectioning the global data to a smaller region centered on the volcano site and patching bad data values. By default, **uni2puff** also converts the temperature (T) data set onto the same grid as the U and V winds, although this is not required to run **puff**.

The output of the **puff** routine are binary ash files. By default, these are in **netcdf** format. Each file contains the state of the ash cloud at some time following the eruption. The file contains header information with eruption parameters and position and size data for each simulated ash particle. The routine **ashdump** displays the data contained in an ash file to stdout in ASCII format.

RUNNING PUFF

All of the **puffsystem** routines accept unix-style command line arguments to alter behavior or set parameter values. There are four types of arguments: *required*, *string*, *double*, *long*, or *flag*. Except for *required* arguments the syntax for argument values are:

```
-argname=argvalue  
-argname argvalue
```

where a minus sign precedes the argument name and either a space or an equal sign separate the value from the name. Argument names are case-sensitive. *string* values should be enclosed with quotes if they contain white space (quotes are ignored). *flag* values may omit the *argvalue* in which case they are taken *true*, otherwise, explicitly set *flag* values with *-argname=true* or *-argname=false*. *required* values exist on the command line alone without a minus sign or an expected value.

All of the **puffsystem** routines accept the flag argument *-help*. Setting this flag displays a usage

Version: 2.0

Last change: May 1996

message and all of the available options with their default values before exiting the routine.

The routines **uni2puff** and **puff** also accept input from a file. By default these routines attempt to read from the file *puff.input*. If this file does not exist, a warning is issued. Arguments are set in a file with almost the same syntax as command line arguments. The only difference is the minus sign '-' is replaced with a backslash '\ ' and arguments should appear on separate lines. Lines beginning with a hatch '#' are ignored by the parser. Arguments set on the command line have precedence over the same arguments appearing in a file. The routine **puffin** prompts the user for input arguments and writes to the file *puff.input*.

The minimum parameters for running **puff** are the time and location of the eruption. The location may be set to one of the pre-compiled volcano names with the *-volc* parameter. The routine **puffin** displays all of the pre-compiled volcano sites. If the volcano of interest is not in this data base, the two parameters *-volcLon* and *-volcLat* must be set. The eruption time is set through the parameter *-eruptDate*. This is a 16-character string in the format "YYYY MM DD HH:MM" and is expected to be in UTC. If no other arguments are present, default values will be used and the routines **uni2puff** and **puff** will attempt to construct the most recent input wind file date using the *-eruptDate* parameter and the file-name parameters *-uniTail* and *-windTail*.

For more details, the user should familiarize themselves with the other options available in the main routines **uni2puff**, **puff**, and **ashview**.

THE PUFF MAN PAGES

This section contains the unix man pages available with the **puffsystem** installation. The main routines are:

ashdump	Formats and displays the contents of a binary ash file
ashview	Creates postscript or image maps of ash data
puff	The main simulation and tracking routine
puffin	Routine to prompt the user for input to the uni2puff and puff routines
runpuff	csh-script to run the routines puffin , uni2puff , puff and ashview
uni2puff	Converts <i>Unidata</i> files to puff format

Additional routines included with the installation are:

ashbin	Calculates gridded concentrations of ash between height levels
fgconv	Utility to convert and manipulate multi-dimensional data sets
fgdump	Utility to display information in multi-dimensional data sets
traject	Runs the puff simulation in trajectory mode
uniconv	Utility to convert and manipulate <i>Unidata</i> files.
unipack	Utility for packing the time dimension of several <i>Unidata</i> files
uniprof	Utility to display vertical profile values at a particular location and time

ASHBIN

NAME

ashbinND - ashbin2D [ashbin3D] bins ash data into a 2D [3D] volume.

OPTIONS

infile *required*
Input ash file

-grid *string* Data lon/lat grid size when -pickGrid=true ["5.0/2.5"]

-range *string*
lonmin/lonmax/latmin/latmax range ["-180/-120/60/75"]

-height *string*
zmin/zmax/[zbin] height bin range ["0/16000/2000"]

-help *flag* Print this summary [false]

ASHDUMP

NAME

ashdump - ashdump prints specific information from an ash binary file. The default is to print everything - format control is achieved with the following:

OPTIONS

- infile** *required*
Input ash file
- lon flag** Print lon field using ashdump [false]
- lat flag** Print lat field using ashdump [false]
- z flag** Print height field using ashdump [false]
- sz flag** Print size field using ashdump [false]
- age flag** Print age field using ashdump [false]
- hdr flag** Print ash header information [false]
- stats flag** Print basic ash stats with ashdump [false]
- active flag** Print only active ash with ashdump [false]
- range string**
Lon/Lat range for read or mapping ["-180/-120/60/75"]
- height string**
Height range /meters/ filter for mapping ["0/20000"]
- size string** Size range filter ["0/1.e30"]
- shiftWest flag**
Shift lon values from -180:180 to 0:360 [true]
- shoparams flag**
Show puff parameters used [false]
- width long** Set width of output in ashdump [14]
- precision lng**
Set precision of output in ashdump [0]
- help flag** Print this summary [false]

Version: 2.0

Last change: 96/05/24

ASHVIEW

NAME

ashview - ashview creates and executes a csh script for postscript and gif output using the GMT software. The script accepts 1 to 5 ash files for overlaying on the plot regin. At least one ash file must be specified.

OPTIONS

- ashfile1** *required*
Ashfile
- ashfile2** *required*
Ashfile
- ashfile3** *required*
Ashfile
- ashfile4** *required*
Ashfile
- ashfile5** *required*
Ashfile
- range** *string*
Output Map range [lonmin/lonmax/latmin/latmax]
- zbin** *string* Height zmax/zmin/dz in meters [2000/18000/4000]
- xsize** *string*
Map width in inches [5.5]
- ticks** *string*
GMT -B tick notation ["]]
- ashpen** *string*
GMT ash pen attributes ["-Sc0.02 -Cashview.cpt"]
- vlcpen** *string*
GMT volcano pen attributes ["-St0.15 -G0"]
- cstpen** *string*
GMT pscoast pen attributes ["-W2 -Di -A250"]
- airpen** *string*
GMT airroutes pen attributes ["-M -A -W3/6/6/6"]
- lshade** *string*
RGB values for land shade ["255/174/116"]

Version: 2.0

Last change: 96/05/24

- oshade string**
RGB values for ocean shade ["209/238/238"]
- kmscale string**
Map scale xpct/ypct/km [0.15/0.15/200]
- simple flag**
Create simplified plot without annotation region [false]
- gif flag** Make GIF output [false]
- dpi string** DPI resolution for -gif output [96]
- bw flag** Make Black/White plot [false]
- noscatter flag**
Do not plot ash points [false]
- traject flag**
Overlay trajectory files [false]
- airroutes flag**
Overlay air routes [false]
- stamp string**
Place a text stamp in trailer ["Ash trajectory and dispersion model
'date'"]
- stampbg string**
Stamp background R/G/B color [230/230/230]
- stampfg string**
Stamp foreground R/G/B color [0/0/0]
- stampfn string**
Stamp region GMT font number [0]
- stampfs string**
Stamp region font size [9]
- headbg string**
Header background R/G/B color [230/230/230]
- headfg string**
Header foreground R/G/B color [0/0/0]
- headfn string**
Header region GMT font number [0]
- headfs string**
Header region font size [11]
- comment string**
Annotation text string: separate lines with '/' [""]
- save flag** Save the intermediary csh script file [false]

- puffdir *string***
Puff directory ["/u1/uaf/csearcy/puff"]
- tmpdir *string***
Temporary directory for output ["/scratch"]
- htmldir *string***
HTML directory for utilites to convert ps to gif ["/usr/local/html"]
- gs *flag*** Use ghostscript instead of html routines to convert .ps to .gif [false]
- gsutil *string***
Ghostscript utility if using -gs ["/usr/local/bin/gs"]
- pstoppm *string***
Ghostscript PSTOPPM file ["/usr/local/lib/ghostscript/pstoppm.ps"]
- ppmtogif *string***
Utility for converting ppm to gif ["/usr/local/bin/imconv"]
- help *flag*** Print this summary [false]

PUFF

NAME

puff - ash tracking software

OPTIONS

- volc** *string* Volcano name ["unknown"]
- volcLon** *double*
Volcano longitude [-9999]
- volcLat** *double*
Volcano latitude [-9999]
- eruptDate** *string*
UTC Eruption date string in format "YYYY MM DD HH:MM"
["YYYY MM DD HH:MM"]
- runHours** *double*
Simulation length in hours [24]
- fileDate** *string*
Unidata file header in format "YYMMDDHH" ["YYMMDDHH"]
- shiftWest** *flag*
Shift longitude values from -180:180 to 0:360 [true]
- windUfile** *string*
Explicitly read/write puff U wind file [""]
- windVfile** *string*
Explicitly read/write puff V wind file [""]
- windTail** *string*
Puff wind file tail where X will be replaced with U or V [".puffX.cdf"]
- argFile** *string*
Read optional arguments from file [""]
- help** *flag* Print this summary [false]
- eruptHours** *double*
Length of eruption in hours [1.e30]
- plumeHeight** *double*
Initial ash height in meters [16000]
- nAsh** *long* Number of Ash particles to track [5000]

Version: 2.0

Last change: 96/05/24

- printHours** *double*
Save ash data every -printHours [-9999]
- eruptSeconds** *long*
Explicitly set eruption length in seconds [-9999]
- runSeconds** *long*
Explicitly set simulation length in seconds [-9999]
- printSeconds** *long*
Explicitly set save interval in seconds [-9999]
- dtSeconds** *long*
Explicitly set step length in seconds [-9999]
- ashLogMean** *double*
Logarithmic ash mean size in meters [-5]
- ashLogSdev** *double*
Logarithmic ash sigma in meters [1]
- saveInitAsh** *flag*
Save the initial ash state if true [false]
- ashJulStyle** *flag*
Create ash file headers using julian date [true]
- ashCDF** *flag*
Save ash data in netcdf format [true]
- plumeShape** *string*
Set the initial column shape: (1 ["linear"])
- plumeZwidth** *double*
Initialize ash vertical spread in meters [3000]
- plumeHwidth** *double*
Initialize ash horizontal spread in meters [0]
- plumeMin** *double*
Minimum plume height when plumeShape=linear [0]
- saveWfile** *flag*
Save the calculated vertical wind object [false]
- dtMins** *double*
Simulation step length in minutes [5]
- diffuseHor** *double*
Horizontal diffusion coefficient [2.e4]
- diffuseVer** *double*
Vertical diffusion coefficient [1.e1]
- runSurface** *flag*
Continue tracking particles at z=0 if true [false]

- noFall *flag*** Do not include fallout in the motion [false]
- spline *flag*** Use Spline technique instead of Nearest Neighbor [false]
- nSpline *string***
Set spline sizes at T/Z/Y/X ["5/5/5/5"]
- runClock *flag***
Optional output timing style [true]
- seed *long*** Set initial random number seed [-9999]
- shotime *flag***
Display CPU time message [false]

FGCONV

NAME

fgconv - converts between various binary multi-dimensional file formats as well as subsectioning and sampling options.

OPTIONS

- infile** *required*
Required input file
- outfile** *required*
Required output file
- var** *string* Read variable named -var [""]
- help** *flag* Print this summary [false]
- argfile** *string*
Reads input parameters from file [""]
- nspline** *string*
Set the number of indices to use for splines [""]
- rebin** *string*
Rebins the input object according to the TOKEN string [""]
- resize** *string*
Resizes the input object with TOKEN string [""]
- scale** *double*
Scales the input object with TOKEN string [0]
- indices** *flag*
Flag to set the rebin string to index values [Default] [true]
- values** *flag* Flag to set the rebin string to real values [false]
- ndims** *string*
Dimension sizes required for binary or ASCII [""]
- in** *string* Force a read format [fg fa cdf hdf bin ascii] [""]
- out** *string* Force a write format [fg fa cdf hdf bin ascii] [""]
- inoffset** *string*
Force input offset style [C or F] [""]

Version: 2.0

Last change: 96/05/24

- outoffset** *string*
Force output offset style [C or F] [""]
- skip** *long* Skip headers: lines for ASCII and bytes for binary [0]
- width** *long* Set field widths for ASCII output [0]
- precision** *long*
Set precision for ASCII output [0]
- left** *flag* Flag to left-adjust on ASCII output [Default] [true]
- right** *flag* Flag to right-adjust on ASCII output [false]
- spline** *flag* Specify to spline instead of nnint [false]
- patch** *flag* Flag to request patching bad data [false]
- patchline** *string*
Token string to set the order for patch scanning [""]
- scaleval** *double*
Multiply all values by constant factor [1]
- addoffset** *double*
Add to all values [-scaleval performed first] [0]
- unidata** *flag*
Flag to read input as a Unidata object [false]
- shiftwest** *flag*
Flag to shift Unidata lon values from -180:180 to 0:360 [false]
- title** *string* Set the object title [""]
- reftime** *string*
Set the object reference time string [""]
- fillvalue** *double*
Set the object fill value [""]
- validrange** *string*
Set the valid range of the variable [""]
- name** *string*
Set the variable name [""]
- units** *string*
Set the variable units [""]
- x1name** *string*
Set the X1 dimension name [""]
- x1units** *string*
Set the X1 dimension units [""]

- x1dimnorm flag**
Flag to normalize the X1 dimension [false]
- x1dimexpand string**
Expand the X1 dimension over range start:end [""]
- x1dimstep string**
Step the X1 dimension over range start:step [""]
- x1dims string**
String to explicitly set X1 dimension values [""]
- x2name string**
Set the X2 dimension name [""]
- x2units string**
Set the X2 dimension units [""]
- x2dimnorm flag**
Flag to normalize the X2 dimension [false]
- x2dimexpand string**
Expand the X2 dimension over range start:end [""]
- x2dimstep string**
Step the X2 dimension over range start:step [""]
- x2dims string**
String to explicitly set X2 dimension values [""]
- x3name string**
Set the X3 dimension name [""]
- x3units string**
Set the X3 dimension units [""]
- x3dimnorm flag**
Flag to normalize the X3 dimension [false]
- x3dimexpand string**
Expand the X3 dimension over range start:end [""]
- x3dimstep string**
Step the X3 dimension over range start:step [""]
- x3dims string**
String to explicitly set X3 dimension values [""]
- x4name string**
Set the X4 dimension name [""]
- x4units string**
Set the X4 dimension units [""]
- x4dimnorm flag**
Flag to normalize the X4 dimension [false]

-x4dimexpand *string*

Expand the X4 dimension over range start:end ["]]

-x4dimstep *string*

Step the X4 dimension over range start:step ["]]

-x4dims *string*

String to explicitly set X4 dimension values ["]]

FGDUMP

NAME

fgdump - prints info about binary multi-dimensional files.

OPTIONS

- infile** *required*
Required input file
- help flag** Print this summary [false]
- fg flag** Read fitGrid format [false]
- fa flag** Read fitArray format [false]
- cdf flag** Read netcdf format [false]
- hdf flag** Read HDF format [false]
- bin flag** Read binary format [false]
- ascii flag** Read ASCII text format [false]
- offset string**
Read either C or F offset style ["C"]
- var string** Read variable named -var [""]
- simple flag**
Simple output style [true]
- info flag** INFO output style [false]
- full flag** Full output style [false]
- simplenostats flag**
Simple no stats output [false]
- fullnostats flag**
Full no stats output [false]
- quick flag** Even simpler output [false]
- quickstats flag**
Show only stats [false]
- column flag**
Column ascii output [false]

Version: 2.0

Last change: 96/05/24

- columnnostats *flag***
Column with no stats [false]
- ndims *string***
Token string required for -bin or -ascii dimensions ["]]
- skip *long*** Skip headers: Lines for -ascii and Bytes for -bin [0]
- width *long*** Set field widths for -ascii output [0]
- precision *long***
Set precision for -ascii output [0]
- left *flag*** Set left-adjust for -ascii output [true]
- right *flag*** Set right-adjust for -ascii output [false]
- spacing *string***
Set spacing chars for -ascii output [" "]

TRAJECT

NAME

traject - Compute single ash particles trajectories. Does not include diffusion or fallout in the ash motion

OPTIONS

- volc** *string* Volcano name ["unknown"]
- volcLon** *double*
Volcano longitude [-9999]
- volcLat** *double*
Volcano latitude [-9999]
- eruptDate** *string*
UTC Eruption date string in format "YYYY MM DD HH:MM"
["YYYY MM DD HH:MM"]
- runHours** *double*
Simulation length in hours [24]
- fileDate** *string*
Unidata file header in format "YYMMDDHH" ["YYMMDDHH"]
- shiftWest** *flag*
Shift longitude values from -180:180 to 0:360 [true]
- windUfile** *string*
Explicitly read/write puff U wind file [""]
- windVfile** *string*
Explicitly read/write puff V wind file [""]
- windTail** *string*
Puff wind file tail where X will be replaced with U or V [".puffX.cdf"]
- argFile** *string*
Read optional arguments from file [""]
- help** *flag* Print this summary [false]
- eruptHours** *double*
Length of eruption in hours [1.e30]
- plumeHeight** *double*
Initial ash height in meters [16000]

Version: 2.0

Last change: 96/05/24

- nAsh** *long* Number of Ash particles to track [5000]
- printHours** *double*
Save ash data every -printHours [-9999]
- eruptSeconds** *long*
Explicitly set eruption length in seconds [-9999]
- runSeconds** *long*
Explicitly set simulation length in seconds [-9999]
- printSeconds** *long*
Explicitly set save interval in seconds [-9999]
- dtSeconds** *long*
Explicitly set step length in seconds [-9999]
- ashLogMean** *double*
Logarithmic ash mean size in meters [-5]
- ashLogSdev** *double*
Logarithmic ash sigma in meters [1]
- saveInitAsh** *flag*
Save the initial ash state if true [false]
- ashJulStyle** *flag*
Create ash file headers using julian date [true]
- ashCDF** *flag*
Save ash data in netcdf format [true]
- plumeShape** *string*
Set the initial column shape: (1 ["linear"])
- plumeZwidth** *double*
Initialize ash vertical spread in meters [3000]
- plumeHwidth** *double*
Initialize ash horizontal spread in meters [0]
- plumeMin** *double*
Minimum plume height when plumeShape=linear [0]
- saveWfile** *flag*
Save the calculated vertical wind object [false]
- dtMins** *double*
Simulation step length in minutes [5]
- diffuseHor** *double*
Horizontal diffusion coefficient [2.e4]
- diffuseVer** *double*
Vertical diffusion coefficient [1.e1]

- runSurface flag**
Continue tracking particles at z=0 if true [false]
- noFall flag** Do not include fallout in the motion [false]
- spline flag** Use Spline technique instead of Nearest Neighbor [false]
- nSpline string**
Set spline sizes at T/Z/Y/X ["5/5/5/5"]
- runClock flag**
Optional output timing style [true]
- seed long** Set initial random number seed [-9999]
- shotime flag**
Display CPU time message [false]

UNI2PUFF

NAME

uni2puff - Converts Unidata files into puff format by converting millibar height to meters; patching bad data; and subsectioning a region.

OPTIONS

- volc** *string* Volcano name ["unknown"]
- volcLon** *double*
Volcano longitude [-9999]
- volcLat** *double*
Volcano latitude [-9999]
- eruptDate** *string*
UTC Eruption date string in format "YYYY MM DD HH:MM"
["YYYY MM DD HH:MM"]
- runHours** *double*
Simulation length in hours [24]
- fileDate** *string*
Unidata file header in format "YYMMDDHH" ["YYMMDDHH"]
- shiftWest** *flag*
Shift longitude values from -180:180 to 0:360 [true]
- windUfile** *string*
Explicitly read/write puff U wind file [""]
- windVfile** *string*
Explicitly read/write puff V wind file [""]
- windTail** *string*
Puff wind file tail where X will be replaced with U or V ["_puffX.cdf"]
- argFile** *string*
Read optional arguments from file [""]
- help** *flag* Print this summary [false]
- path** *string*
Set path for reading Unidata files [""]
- uniTail** *string*
Unidata file tail substituting U/V/H/T for X ["_avn-X.cdf"]

Version: 2.0

Last change: 96/05/24

- pickGrid** *flag*
Automatic lon/lat grid generation [true]
- ngrid** *string*
Size of lon/lat grid when -pickGrid=true ["45/30"]
- grid** *string* Data lon/lat grid size when -pickGrid=true ["1.25/1.25"]
- range** *string*
Read grid: "t1:t2/z1:z2/y1:y2/x1:x1" [""]
- vars** *string* Unidata variables to convert ["H/U/V/T"]
- varnames** *string*
Unidata arg(vars ["Z/u/v/T"])
- Hsimple** *flag*
Use a simple PtoH conversion without the H file [false]
- Hconst** *double*
RT/g Factor used when -Hsimple=true [7400]
- P0** *double* Surface pressure in millibars when -Hsimple=true [1000]
- patch** *string*
Unidata patching scan direction ["TZYX"]
- uniHfile** *string*
Explicitly read unidata H file [""]
- uniUfile** *string*
Explicitly read unidata U file [""]
- uniVfile** *string*
Explicitly read unidata V file [""]
- uniTfile** *string*
Explicitly read unidata T file [""]

UNICONV

NAME

uniconv - subsection and patch a Unidata file and/or convert pressure levels

OPTIONS

- infile** *required*
Required input file
- outfile** *required*
Required output file
- var** *string* Read variable -var [""]
- range** *string*
Subset range t1:t2/z1:z2/y1:y2/x1:x2 ["*/*/*"]
- shiftwest** *flag*
Convert longitude values to 0:360 [true]
- Hfile** *string*
Convert vertical level using H-file interpolation [""]
- Hsimple** *flag*
Convert vertical level to meters using simple approximation [false]
- P0** *double* Surface pressure used in millibars when -Hsimple=true [1000.0]
- Hconst** *double*
RT/g Factor used when -Hsimple=true [7400]
- patch** *flag* Patch bad values [false]
- help** *flag* Print this summary [false]

UNIPACK

NAME

unipack - updates latest file with forecast or measured data from previous cycles to create a file "file1.pack.cdf"

OPTIONS

infile *required*

Required input file - multiple files accepted

-measured *flag*

packs only measured data from all data [true]

-zero *flag* packs only measured data from all early data while including forecast data from latest file [false]

UNIPROF

NAME

uniprof - Display vertical profile data from a 4D Unidata set

OPTIONS

-lon *double* site longitude []

-lat *double* site latitude []

-date *string*reftime date string in format "YYYY MM DD HH:MM" []